Structural size effect: Experimental, theoretical and accurate computational assessment

G. B. Barbat, M. Cervera, M. Chiumenti and E. Espinoza

International Center for Numerical Methods in Engineering (CIMNE)

Technical University of Catalonia – BarcelonaTECH

Edificio C1, Campus Norte, Jordi Girona 1-3

08034 Barcelona, Spain

gbarbat@cimne.upc.edu, miguel.cervera@upc.edu, michele@cimne.upc.edu, edu.espinoza.duran@gmail.com

Abstract

In this paper, experimental evidence, theoretical predictions and the finite element modelling of the structural size effect in cracking problems of quasi-brittle materials are discussed and assessed against each other. The fracture process is modelled through the crack band approach, using an isotropic damage constitutive law. The correct dissipation of the fracture energy, essential for modelling the phenomenon with precision, is introduced. An enhanced accuracy mixed finite element formulation is used to ensure mesh bias independent results. Several experimental campaigns where size effect is investigated are numerically reproduced in 2D and in 3D to assess the feasibility and the performance of the method. For this, mode I and mixed mode I and II fracture situations are considered in notched and unnotched beams. The correlation of the experimental results with the numerical simulations shows the capacity of the mixed FE formulation to reproduce crack paths, force-displacement curves and collapse mechanisms with precision for a wide range of structural sizes. The enhanced accuracy FE formulation eliminates the spurious mesh dependency that is characteristic of standard FE simulations. In addition, the model is able to follow Bazant's size effect law with precision. Results confirm that the energy release rate in the progressing fracture is the fundamental cause of size effect in quasi-brittle materials. This is additionally verified in a study of the relative influence of statistical and energetic size effect. Computations show that the essential requirements to suitably simulate the phenomenon are (1) a fracture model ensuring the correct energy dissipation at the crack and (2) a method guaranteeing mesh objective results.

Keywords: Cracking, Size Effect, Damage, Fracture Energy, Strain Localization, Mixed Finite Elements

1. Introduction

Structural size effect refers to the variation, motivated by a change of size, of the load capacity of a structure from estimations made using stress failure criteria [1]. The observed behavior of quasi-brittle specimens in laboratory tests does not correlate with the one perceived in real sized structures, because the latter are usually much bigger. This phenomenon has a profound impact in many practical applications such as in concrete structures, as evidenced by its incorporation into the 2019 version of the American Concrete Institute design norm for structural concrete [2], but also in geomechanics, composite materials or artic ice engineering among others [3, 4].

In order to take into consideration the physical phenomenon of size effect in engineering applications the use of numerical modelling is required. Both by academics and practitioners, the most widely used strategy to analyze fracture and structural failure with the finite element method is the smeared crack approach, introduced more than 50 years ago by Rashid [5] and adopted in this work. Within this approach, the fracture is modeled through the degradation of the material at the constitutive level.

Specifically, the crack band theory (CBT), introduced by Bazant in [6], is considered herein. CBT consists in regularizing, or "smearing", the displacement jump across a zero thickness crack into the corresponding nominal strains across a band of small, but finite, thickness. Consistency and, therefore, convergence, of the derived FE approach depends on two factors. On the one hand, the regularization of a discontinuous displacement field needs to be proved consistent at continuum level, before FE discretization is performed. This consistency is discussed in [7, 8], where, among other requirements, it is shown that to ensure correct energy dissipation when the cohesive crack opens it is necessary to relate, at continuum level, the cohesive behavior of the regularized crack, i.e. its softening behavior, to the actual width of the band. As will be discussed in detail in Section 2, achieving the proper energy dissipation when the crack is developing is an essential requirement for the correct assessment of the size effect phenomenon [4, 9, 10, 11]. On the other hand, the FE discrete problem needs to be consistent with the regularized continuum one. This requires from the FE formulation to relate the width of the crack to the size of the FE mesh. Therefore, the required adjustment of the softening behavior of the material with respect to the bandwidth of the regularized crack at continuum level, translates, when introducing the FE discretization, to its correction with respect to the FE size. This avoids spurious mesh size dependent results, as intended when the crack band theory was introduced in [6].

Notwithstanding the mesh size representation, the main difficulty posed by the smeared crack approach and the crack band theory, when applied with standard displacement-based FEs, is the spurious mesh dependency that it suffers when computing crack trajectories. However, mesh-bias independence is an indispensable requirement of the numerical model. Firstly, for a given structural size, the failure mechanism predicted by the numerical model must be the same independently of the FE mesh used in the analysis. Otherwise, the numerical solution is, in plain terms, useless. Secondly, and regarding size effect specifically, significant variations in the brittleness of the structural behavior caused by the changes in size may cause significant changes in the development of the collapse mechanism [11]. To overcome the lack of mesh-objectivity displayed by the smeared crack method in some situations, auxiliary crack tracking techniques have been proposed and successfully applied [12, 13].

Because of this drawback of the crack band theory, several alternative techniques have been proposed over the last decades to avoid mesh bias dependency in fracture problems. Gradient enhanced [14, 15, 16], nonlocal [17, 16] and phase-field models [15, 18, 19, 20] have been used to avoid spurious mesh-dependency of the computed results in terms of the crack path. However, these techniques use a localization limiter dependent on an internal length that

governs the size of the crack band width. As it has been emphasized in [21], a clear physical interpretation and direct link between the length parameter in the model and the characteristic length of the material is arguable. “Geometrically” regularized gradient-damage [22] and phase-field models [23, 24, 25] have been recently proposed. However, the practical use of all these methods is limited to specific situations and constitutive behaviors.

It has been shown in previous works [26, 27] that in cracking problems of quasi-brittle materials, the mesh dependency of the standard displacement-based FE formulation in solid mechanics is in fact caused by their lack of local convergence in the computed stress and strain fields. This is especially harmful because the trajectory is determined by the stresses and strains that develop in quasi-singular points near the tip of the propagating crack. The stress and strain at these points may be inaccurately computed, averting the correct computation of the crack trajectory.

In this work, the issue of spurious mesh-dependency is addressed through an enhanced-accuracy mixed strain/displacement FE formulation, proposed and developed in references [26, 27, 28, 29, 30, 31, 32]. In the mixed FE formulation, strains are additional nodal unknowns of the FE problem, as well as the nodal displacements. This provides an independent discrete interpolation of the strain field, instead of being computed at element level by discrete differentiation. This kinematic enhancement increases the rate of convergence of the strain and stress fields. Their local and global convergence is ensured in the quasi-singular situations that arise near the tip of the progressing crack. The spurious mesh dependency and lack of local convergence which hamstrings cracking problems solved with standard FE is prevented. In this way, it is possible to obtain accurate results in terms of fracture paths without the use of any crack tracking technique and with far coarser mesh densities than the ones required in phase-field formulations.

In previous works, the authors have demonstrated the use of mixed displacement/pressure FE to assess structural size effect in relation to mode II failure [11] and also shown the enhanced accuracy and mesh-objectivity achievable by the mixed strain/displacement FE in mode I and mixed mode fracture. Ensuingly, in this work, the strain/displacement mixed formulation is applied to assess structural size effect in mode I and mixed mode fracture situations.

A classical local damage constitutive law is employed to represent cracking in quasi-brittle materials. To model mode I and mixed mode I and II fracture, isotropic Rankine damage is considered. The nonlinear behavior of the material is characterized by two parameters: the (tensile) strength and the fracture energy. The capacity of the proposed constitutive law to reproduce size effect, including the perfectly ductile and perfectly brittle limits, is investigated. The bandwidth of the crack is set in function of the finite element size. It is determined by the resolution of the FE only, as required in the crack band method [6].

The objectives of this work are: (1) to establish the necessary and sufficient features required in a constitutive law for modelling the size effect phenomenon, (2) to show the performance of the proposed model in reproducing results consistent with documented data with regard collapse mechanisms, force-displacement curves and crack trajectories for a wide range of structural sizes, (3) to demonstrate the capability of the mixed FE formulation in producing precise and mesh independent results, (4) to show that the main and dominant influencing factor of size effect in quasi-brittle materials is the release of stored energy of the structure, (5) to demonstrate the performance of the model in accurately reproducing Bazant’s size effect law over a wide range of structural sizes.

The outline of this paper is as follows. In Section 2 structural size effect is introduced. In Section 3 the isotropic damage constitutive model used in this work is described. In Section 4 the mixed FE formulation employed to obtain mesh-bias independent results with enhanced

accuracy is outlined. Section 5 presents the numerical simulations of several experimental campaigns where the capacity of the model in reproducing the size effect phenomenon is thoroughly analyzed. In Section 6 a mesh-sensitivity study is performed to show the aptness of the model in producing results without spurious mesh dependence. In Section 7 the relative influence of the statistical variability of the mechanical properties of the material as a source of size effect is assessed. In Section 8 the ability of the model in reproducing Bazant's size effect law is investigated. Finally, some conclusions are given in Section 9.

2. **Structural size effect**

In this section, theoretical and practical considerations regarding structural size effect are given. According to Bazant [1, 3], several sources of structural size effect have been observed:

- Release of stored energy
- Statistical size effect
- Boundary layer effect
- Diffusion phenomena
- Hydration heat

However, not all these sources have the same influence in the phenomenon. Undoubtedly, the most important one is, by far, the release of stored energy. In quasi-brittle problems, the relative influence of statistical size effect is considered unimportant when compared to the effect that the release of the stored energy has in the overall phenomenon. The last three sources are deemed to have only a secondary impact and can be effectively neglected in laboratory tests where specimens have a constant thickness for all the sizes [1, 4].

Therefore, the study of the size effect phenomenon is principally related to energetic considerations [4, 9, 10, 11]. When the fracture develops the stored elastic energy in the structure is released into the crack front. This energy is dissipated and engaged into the process of the crack surface formation. The ratio between the elastic energy stored in the structure and the energy dissipated through the crack tip varies when size changes. This is the main cause for structural size effect. These energetic considerations also govern the relative extent of the fracture process zone within the structure. In plasticity theory, the size of the process zone is of the order of the structural size. The classical linear elastic fracture mechanics (LEFM) theory is developed under the hypothesis that the fracture process zone is negligible with respect to the structural size. For actual quasi-brittle materials, the extent of the fracture process zone cannot be neglected and it grows significantly when size decreases.

According to the dimensional analysis derived in reference [11], in situations involving materials with softening, the brittleness of the problem is governed by the brittleness number Π_B, the ratio D/L between the characteristic size of the structure D and the material characteristic length L, which depends only on the material properties. Irwin's characteristic length L is equal to

$$L = \frac{EG_f}{(f_t)^2} \tag{1}$$

where E is Young's modulus, f_t is the (tensile) strength and G_f is the fracture energy of the material, which is the energy dissipated per unit of area of the fracture surface. Thus, from energy considerations, the brittleness of the problem is size-dependent.

Consequently, collapse in smaller specimens occurs in a more ductile way while larger specimens fail in a more brittle manner. In the small limit case, the formation of a failure

mechanism takes place as a result of the yielding of an extensive area. In the large scale limit, perfect brittle failure occurs. For intermediate sizes failure is due to the formation of a crack that gradually develops in the structure while stress redistribution and the release of stored energy into the crack front takes place [1, 10].

From experimental observations and theoretical considerations [9] Bazant's size effect law has been proposed to represent the phenomenon. It describes the relationship between the load capacity of the structure and its characteristic size. It is defined in its simplest form as [1]:

$$\sigma_{N_u} = B f_t \left(1 + \frac{D}{D_0}\right)^{-\frac{1}{2}} \tag{2}$$

where σ_{N_u} is the nominal strength, defined as

$$\sigma_{N_u} = c_n \frac{P_u}{Db} \quad \text{(2D Scaling)}; \qquad \sigma_{N_u} = c_n \frac{P_u}{D^2} \quad \text{(3D Scaling)} \tag{3}$$

where D is the characteristic size of the structure, b is its thickness, P_u is the ultimate/failure load of the structure, f_t is the strength of the material and D_0 is a reference structural size; B is a dimensionless constant which depends on the shape and the loading of the structure but not on its size and c_n is a dimensionless constant that can be arbitrarily chosen. The law in Eq. (2) is only valid for quasi-brittle materials over a limited range of D. Modifications have been proposed in references [1, 33] to account for larger ranges of sizes and also for the particular case of unnotched structures. This law has been introduced in the 2019 version of the ACI code for structural concrete [2] for revising the strength of concrete in some situations through the inclusion of a size effect modification factor. In [2], which is intended for design purposes, D_0 for concrete is taken as $10\ in = 0.254\ m$.

Assuming that the reference structural size D_0 is linearly dependent with Irwin's characteristic length L, $D_0 = A^{-2}L$, A being a constant similar to B, allows to rewrite Bazant's law in Eq. (2) as

$$\begin{aligned} \sigma_{N_u} &= B f_t \left(1 + A^2 \frac{D}{L}\right)^{-\frac{1}{2}} \\ &= B f_t (1 + A^2 \Pi_B)^{-\frac{1}{2}} \end{aligned} \tag{4}$$

where $\Pi_B = D/L$ is the brittleness number defined in [11].

In Figure 1 the size effect behavior described by Bazant's law in Eq. (2) is shown, where the role of the reference size D_0 is appreciated. The law indicates how for small structures, when D/D_0 is much smaller than 1, $\Pi_B \to 0$, the structure collapses following the predictions of limit analysis, which does not contemplate size effect, as the nominal strength of the material is constant with size: $\sigma_{N_u}(\Pi_B \to 0) = B f_t$. For large structures, when D/D_0 is much larger than 1, $\Pi_B \to \infty$, the structure fails following the LEFM theory, with the strongest possible size effect, the nominal strength being inversely proportional to the square root of the structural size [3]: $\sigma_{N_u}(\Pi_B \to \infty) = (B/A)\sqrt{E G_f}(D)^{-1/2}$ It can be seen that in large notched specimens, where stress singularities exist, a failure criterion expressed in terms of maximum stress is not adequate. In such cases, an energy failure criterion such as the one introduced in LEFM is applicable. For intermediate cases a gradual transition from one failure mode to the other takes place, as it typically happens in most applications involving quasi-brittle fracture [10].

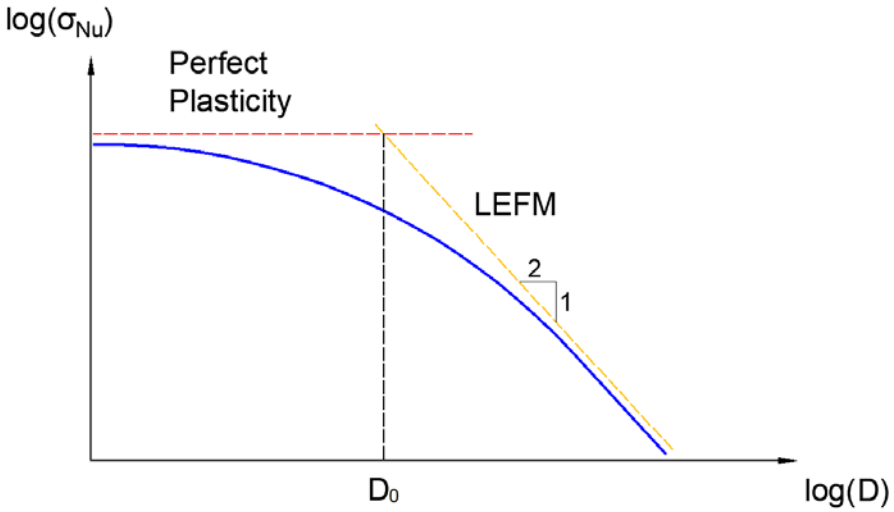

Figure 1. Bazant's size effect law

It is noteworthy that even though the size effect law is generally defined in terms of the nominal strength σ_{N_u}, this is in fact an indirect way of describing the peak load P_u sustainable by the structure in terms of its characteristic size. Therefore, the nominal stress is not a real stress but a load parameter, useful to depict in a clearer way the deviation from limit analysis due to size effect [4].

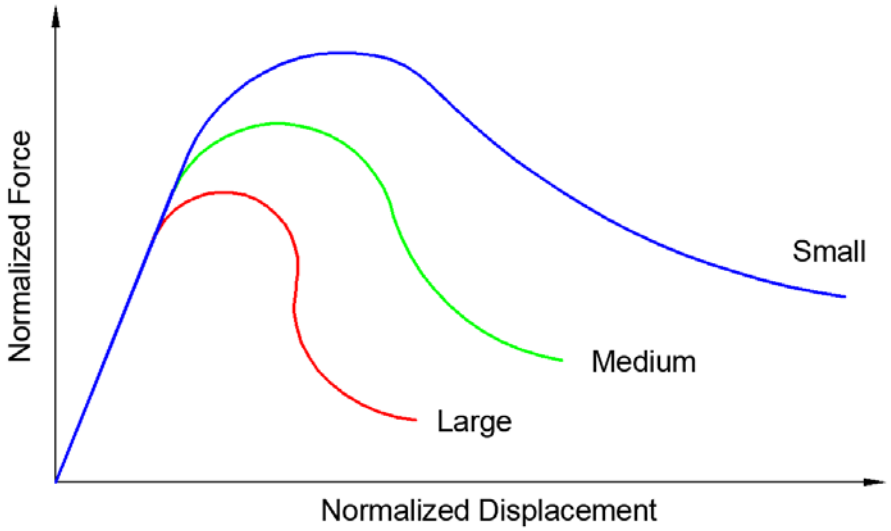

Figure 2. Force-displacement curves, normalized with size, of geometrically similar structures exhibiting size effect

Experimental evidence shows that, in addition to the consequences that it has on the structural load capacity, size effect also governs the ductility and post-peak behavior of the structure. For loading under displacement control, failure in larger sized structures occurs closer to the peak load [1, 3], as shown in Figure 2. The fact that the post-peak curves of large structures descend more steeply than in smaller ones [4, 10] is also due to the fact that, once properly normalized, the energy dissipated in the failure process is comparatively smaller in larger structures.

When considering the scaling of structures in general, several other factors do not scale geometrically apart from their brittleness. For example, in dynamic analysis, a big concern is the fact that the strain rate is influenced by the scaling factor, affecting the predictions of the stresses obtained from scaled models [34, 35, 36]. This issue, which requires specific attention, is not treated in this work which focusses on structural size effect under quasi-static loading. It

should also be noted that weight forces do not scale geometrically neither. Even if considering them in FE analysis is straightforward, they can be effectively neglected in laboratory tests of small concrete specimens. Regarding scale modelling, it should also be taken into consideration that in laboratory tests the possibilities of scaling the aggregate inside concrete are limited.

3. **Isotropic damage model**

In this section, the formulation of the isotropic damage constitutive law is presented. Employing Voigt's convention, the strain and stress tensors are represented as vectors. In 3D the strain vector is $\boldsymbol{\varepsilon} = \left(\varepsilon_x, \varepsilon_y, \varepsilon_z, \gamma_{xy}, \gamma_{xz}, \gamma_{yz}\right)^T$ and stress vector is $\boldsymbol{\sigma} = \left(\sigma_x, \sigma_y, \sigma_z, \tau_{xy}, \tau_{xz}, \tau_{yz}\right)^T$. In an isotropic damage model $\boldsymbol{\varepsilon}$ and $\boldsymbol{\sigma}$ are linked through the constitutive equation:

$$\boldsymbol{\sigma} = \mathbf{D}(d)\,\boldsymbol{\varepsilon} = (1-d)\mathbf{D}_0\,\boldsymbol{\varepsilon} \tag{5}$$

Energy dissipation, size effect and FE meshes

Regarding energy dissipation, at the continuum level, when considering non-regularized cracks, the total energy dissipated during the fracture process is proportional to the area of the crack surface. However, when the regularization of the cracks is introduced, at continuum level, the total energy dissipation is proportional to the volume of the localization band [7, 8]. Therefore, for ensuring consistency between the regularized and non-regularized problems, the fracture energy per unit area G_f is substituted by $g_f = \mathrm{G}_f/b$ as the energy dissipated by unit volume, b being the width of the regularized crack. In such case, the same brittleness number as in the original problem holds

$$\Pi_B = \frac{D}{b}\cdot\frac{b}{L} = \frac{D}{L} \tag{6}$$

In the discrete FE problem, the crack bandwidth b is related to the FE size h ($b = \alpha h$, α being a constant, $\alpha = 1$ for standard FE, $\alpha = 2$ for mixed FE) and the same brittleness number is recovered

$$\Pi_B = \frac{D}{\alpha h}\cdot\frac{\alpha h}{L} = \frac{D}{L} \tag{7}$$

guaranteeing the consistency between the continuum and the discrete problems with respect to fracture energy dissipation and mesh-size objectivity.

Therefore, if structural size effect is investigated by increasing D while the ratio D/h fixed (that is, scaling the mesh with the structural size), brittleness is exactly expressed by the ratio h/L, where h increases in the same way as D.

Let $\Pi_0 = D_0/L$ be the brittleness of the reference size D_0 and the scale $s = D/D_0$. Then, for a size D

$$\Pi_B = \frac{D}{L} = \frac{D_0}{L}\cdot\frac{D}{D_0} = \Pi_0 \cdot s \tag{8}$$

When the ratio D/h is fixed, $D/h = D_0/h_0$ is constant, h_0 being the corresponding FE size when $D = D_0$, and

$$\Pi_B = \frac{D}{L} = \frac{D_0}{L}\cdot\frac{D}{D_0} = \frac{D_0}{L}\cdot\frac{h}{h_0} = \Pi_0 \cdot s \tag{9}$$

So, in such case, the scale s is determined by the actual size of the structure or the finite elements, as $s = D/D_0 = h/h_0$.

4. Mixed FE formulation

In this work a mixed **ε/u** formulation is adopted to solve the mechanical problem with enhanced accuracy. Apart from other strong points, this formulation avoids the spurious mesh dependency that is characteristic in fracture simulations of quasi-brittle materials. In this section, the mixed FE formulation used to compute all the simulations in this work is briefly presented. The formulation is fully described in reference [29]. For additional details, references [26, 27, 28, 30, 32, 38] are recommended.

In this technique, the variational form of the nonlinear solid mechanics problem is posed considering the displacements $\boldsymbol{u}$ and the strains $\boldsymbol{\varepsilon}$ as unknowns. Following Voigt's notation, the compatibility equation relates the strain and displacement fields

$$\boldsymbol{\varepsilon} = \mathbf{S}\,\boldsymbol{u} \tag{10}$$

where **S** is the differential symmetric gradient operator. In addition, the stress vector $\boldsymbol{\sigma}$ and the body forces vector **f** are linked through the Cauchy momentum equation, written in matrix form as

$$\mathbf{S}^T\boldsymbol{\sigma} + \mathbf{f} = \mathbf{0} \tag{11}$$

where $\mathbf{S}^T$ is the differential divergence operator, adjoint to the **S** in Eq. (15). The constitutive equation connects the stress and strain vectors

$$\boldsymbol{\sigma} = \mathbf{D}\,\boldsymbol{\varepsilon} \tag{12}$$

where **D** is the appropriate secant matrix. It is a thermodynamic requirement that **D** is symmetric.

By pre-multiplying Eq. (15) by the secant matrix **D** and substituting Eq. (17) into Eq. (16) a system of two equations is derived

$$-\mathbf{D}\boldsymbol{\varepsilon} + \mathbf{D}\mathbf{S}\boldsymbol{u} = \mathbf{0} \tag{13}$$

$$\mathbf{S}^T(\mathbf{D}\boldsymbol{\varepsilon}) + \mathbf{f} = \mathbf{0} \tag{14}$$

Eqs. (18)-(19) compose the strong form of the mixed $\boldsymbol{\varepsilon}/\boldsymbol{u}$ formulation together with the proper boundary conditions. The problem is symmetric.

The weak form of the problem is attained by multiplying Eqs. (18) and (19) by the virtual strain $\delta\boldsymbol{\varepsilon}$ and displacement vector $\delta\boldsymbol{u}$ respectively. Then the system is integrated over the spatial domain and the Divergence Theorem is utilized in the right hand side of the second integral operation. The variational form that ensues is

$$-\int_\Omega \delta\boldsymbol{\varepsilon}^T\mathbf{D}\boldsymbol{\varepsilon}\,\mathrm{d}\Omega + \int_\Omega \delta\boldsymbol{\varepsilon}^T\mathbf{D}\mathbf{S}\boldsymbol{u}\,\mathrm{d}\Omega = 0 \quad \forall\delta\boldsymbol{\varepsilon} \tag{15}$$

$$\int_\Omega (\mathbf{S}\delta\boldsymbol{u})^T(\mathbf{D}\boldsymbol{\varepsilon})\,\mathrm{d}\Omega = \int_\Omega \delta\boldsymbol{u}^T\mathbf{f}\,\mathrm{d}\Omega + \int_{\Gamma_t} \delta\boldsymbol{u}^T\bar{\boldsymbol{t}}\,d\Gamma \quad \forall\delta\boldsymbol{u} \tag{16}$$

The variational form of the problem is to find the solutions $\boldsymbol{u}$ and $\boldsymbol{\varepsilon}$ that fulfill the system of Eqs. (20) and (21) and that comply with the boundary condition $\boldsymbol{u} = \mathbf{0}$ on Γ_u, for the arbitrary

virtual displacements $\delta \boldsymbol{u}$, which becomes null on Γ_u, and the arbitrary virtual strains $\delta \boldsymbol{\varepsilon}$. This variational problem is symmetric.

To obtain the discrete form of the mixed problem the spatial domain Ω is discretized into nonoverlapping FE Ω_e, so that $\Omega = \cup\, \Omega_e$. The displacement $\boldsymbol{u}$ and the strain $\boldsymbol{\varepsilon}$ are replaced with the FE discrete approximations $\hat{\boldsymbol{u}}$ and $\hat{\boldsymbol{\varepsilon}}$ defined element-wise as

$$\boldsymbol{u} \cong \hat{\boldsymbol{u}} = \boldsymbol{N}_u \boldsymbol{U} \tag{17}$$

$$\boldsymbol{\varepsilon} \cong \hat{\boldsymbol{\varepsilon}} = \boldsymbol{N}_\varepsilon \boldsymbol{E} \tag{18}$$

where $\boldsymbol{U}$ and $\boldsymbol{E}$ are vectors incorporating the values of the displacements and the strains at the nodes of the finite element mesh. $\boldsymbol{N}_u$ and $\boldsymbol{N}_\varepsilon$ are the matrices incorporating the interpolation functions adopted in the FE approximation.

Using equal interpolation functions for $\boldsymbol{N}_u$ and $\boldsymbol{N}_\varepsilon$ does not conform with the Inf-Sup condition [39, 40, 41]. In this case a stabilization method becomes necessary to ensure the solvability, uniqueness and stability of the discrete mixed problem. The basis of the stabilization procedure is the modification of the discrete variational form using the Orthogonal Subscales Method, introduced within the framework of the Variational Multiscale Stabilization methods and adopted herein [42].

The stabilization strategy is solely to change the approximation of the discrete strain in Eq. (23) by the following discrete field

$$\boldsymbol{\varepsilon} \cong \hat{\boldsymbol{\varepsilon}} = \boldsymbol{N}_\varepsilon \boldsymbol{E} + \tau_\varepsilon (\boldsymbol{B}_u \boldsymbol{U} - \boldsymbol{N}_\varepsilon \boldsymbol{E}) = (1 - \tau_\varepsilon) \boldsymbol{N}_\varepsilon \boldsymbol{E} + \tau_\varepsilon \boldsymbol{B}_u \boldsymbol{U} \tag{19}$$

where τ_ε is a stabilization parameter with value $0 \leq \tau_\varepsilon \leq 1$. Note that for $\tau_\varepsilon = 1$, the strain interpolation of the standard irreducible formulation is regained:

$$\boldsymbol{\varepsilon} \cong \hat{\boldsymbol{\varepsilon}} = \boldsymbol{B}_u \boldsymbol{U} \tag{20}$$

where $\boldsymbol{B}_u$ is the discrete strain-displacement matrix defined as $\boldsymbol{B}_u = \boldsymbol{S}\boldsymbol{N}_u$.

The corresponding algebraic system of equations reads:

$$\begin{bmatrix} -\boldsymbol{M}_{\boldsymbol{\tau}} & \boldsymbol{G}_{\boldsymbol{\tau}} \\ \boldsymbol{G}_{\boldsymbol{\tau}}^T & \boldsymbol{K}_{\boldsymbol{\tau}} \end{bmatrix} \begin{bmatrix} \boldsymbol{E} \\ \boldsymbol{U} \end{bmatrix} = \begin{bmatrix} \boldsymbol{0} \\ \boldsymbol{F} \end{bmatrix} \tag{21}$$

where $[\boldsymbol{E} \quad \boldsymbol{U}]^T$ is the array of nodal values of strains and displacements, and $\boldsymbol{M}_{\boldsymbol{\tau}} = (1 - \tau_\varepsilon)\boldsymbol{M}$, $\boldsymbol{G}_{\boldsymbol{\tau}} = (1 - \tau_\varepsilon)\boldsymbol{G}$ and $\boldsymbol{K}_{\boldsymbol{\tau}} = \tau_\varepsilon \boldsymbol{K}$. $\boldsymbol{M}$ is a mass like projection matrix, $\boldsymbol{G}$ is the discrete gradient matrix, $\boldsymbol{K}$ is a stiffness like matrix and $\boldsymbol{F}$ is the vector of external nodal forces.

$$\boldsymbol{M} = \int_\Omega \boldsymbol{N}_{\boldsymbol{\varepsilon}}^{\boldsymbol{T}} \mathbf{D} \boldsymbol{N}_{\boldsymbol{\varepsilon}} \, \mathrm{d}\Omega \tag{22}$$

$$\boldsymbol{G} = \int_\Omega \boldsymbol{N}_{\boldsymbol{\varepsilon}}^{\boldsymbol{T}} \mathbf{D} \boldsymbol{B}_{\boldsymbol{u}} \, \mathrm{d}\Omega \tag{23}$$

$$\boldsymbol{K} = \int_\Omega \boldsymbol{B}_u^T \mathbf{D} \boldsymbol{B}_u \, \mathrm{d}\Omega \tag{24}$$

$$\boldsymbol{F} = \int_\Omega \boldsymbol{N}_{\boldsymbol{u}}^{\boldsymbol{T}} \boldsymbol{f} \, \mathrm{d}\Omega + \int_{\Gamma_t} \boldsymbol{N}_{\boldsymbol{u}}^{\boldsymbol{T}} \bar{\boldsymbol{t}} \, \mathrm{d}\Gamma \tag{25}$$

5. Numerical analysis of notched and unnotched concrete beams

In this section the experimental campaigns reported in references [43, 44, 45] are numerically investigated. In these laboratory experiments multiple series of geometrically similar notched and unnotched beams of varying sizes are tested. The objective of this section is to show the capacity of the proposed model in accurately reproducing the size effect phenomenon in quasi-brittle materials in mode I and mixed mode I and II fracture.

The simulations are conducted with an enhanced version of the finite element code COMET [46]. Pre- and post-processing are realized with GID [47], developed at CIMNE (International Center for Numerical Methods in Engineering). At each load step increment convergence is attained when the ratio between the norm of residual forces and the norm of total external forces is lower than 10^{-3} %. In all the simulations shown in this work, a stabilization parameter $\tau_\varepsilon = 0.1$ is used.

5.1. Analysis of the Grégoire tests: mode I fracture

In this section, the numerical simulation of the tests of the Grégoire concrete beams is presented. The experiments are reported in [43], which also computed numerical simulations with a non-local model. Other numerical results are also reported in reference [25], where a phase-field model is employed, in [48], where interface elements are used, in [49], where the beam-particle approach is applied, in [50], where the discrete element method is considered and in [51], where a gradient damage model is adopted.

Three-point bending tests of notched and unnotched beams were carried out. The experiments were performed for geometrically similar beams of varying depths D = 400 mm, 200 mm, 100 mm and 50 mm while the span-to-depth ratio was kept constant to 2.5. Several series of beams were tested, with different notch configurations. Specifically, beams with notch-to-depth ratios λ of 0.5 (half-notched), 0.2 (fifth-notched) and 0 (unnotched) were considered. All the beams had the same constant thickness of 50 mm for all the sizes. The details of the geometry of the beams are shown in Figure 3. The material parameters employed in the present simulations are given in Table 1. They have been calibrated by reverse fitting, and they are within a 10% variation to the values recorded from the experimental tests and the ones used in the corresponding reported numerical simulations in [25]. A vertical load is applied at the midpoint of the beams. The analyses are performed under CMOD (crack mouth opening displacement) control.

The case of notch-to-depth ratio of 0.5 is solved under the plane stress hypothesis using a structured mesh. Quadrilateral elements of a size of $1.25 \cdot 10^{-2} D$ are employed, resulting in a total of 22440 elements. The notch width is set equal to the width of one finite element, as shown in Figure 4. Note that this is the maximum mesh size fit to model the evolution of the fracture with the crack band approach. For the other notch configurations, the same FE size is fixed and similar meshes of 22464 and 22480 quadrilateral elements ensue.

Figure 5 shows the force-CMOD curves obtained. It can be seen how the peak load is very similar to the experimental results of [43] for all the sizes of the three series (the half-notched, fifth notched and unnotched beams). In addition, the computed post-peak softening behavior is also very close to the experimental envelopes in all the cases. The overall size effect phenomenon observed in the experiments is well captured by the model using the same material properties in all the simulations. In addition, the same set of material properties model reproduce well the behavior of the three series of beams with different notch-to-depth ratios.

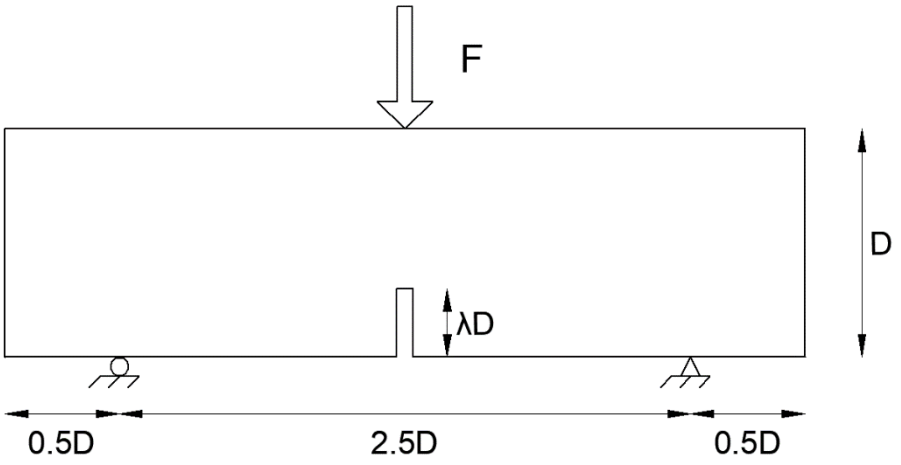

Figure 3. Geometry of the Grégoire experimental tests

Young's Modulus	$37.0 \cdot 10^9$ Pa
Poisson's Ratio	0.2
Tensile Strength	$3.5 \cdot 10^6$ Pa
Tensile Fracture Energy	90 J/m^2
Irwin's material length	0.2718 m

Table 1. Material parameters of the Grégoire tests

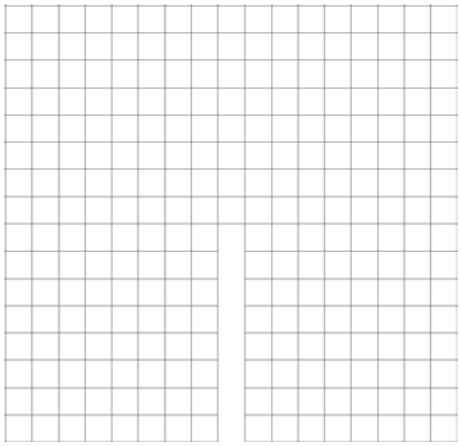

Figure 4. Detail of the mesh used for the Grégoire tests around the tip of the notch

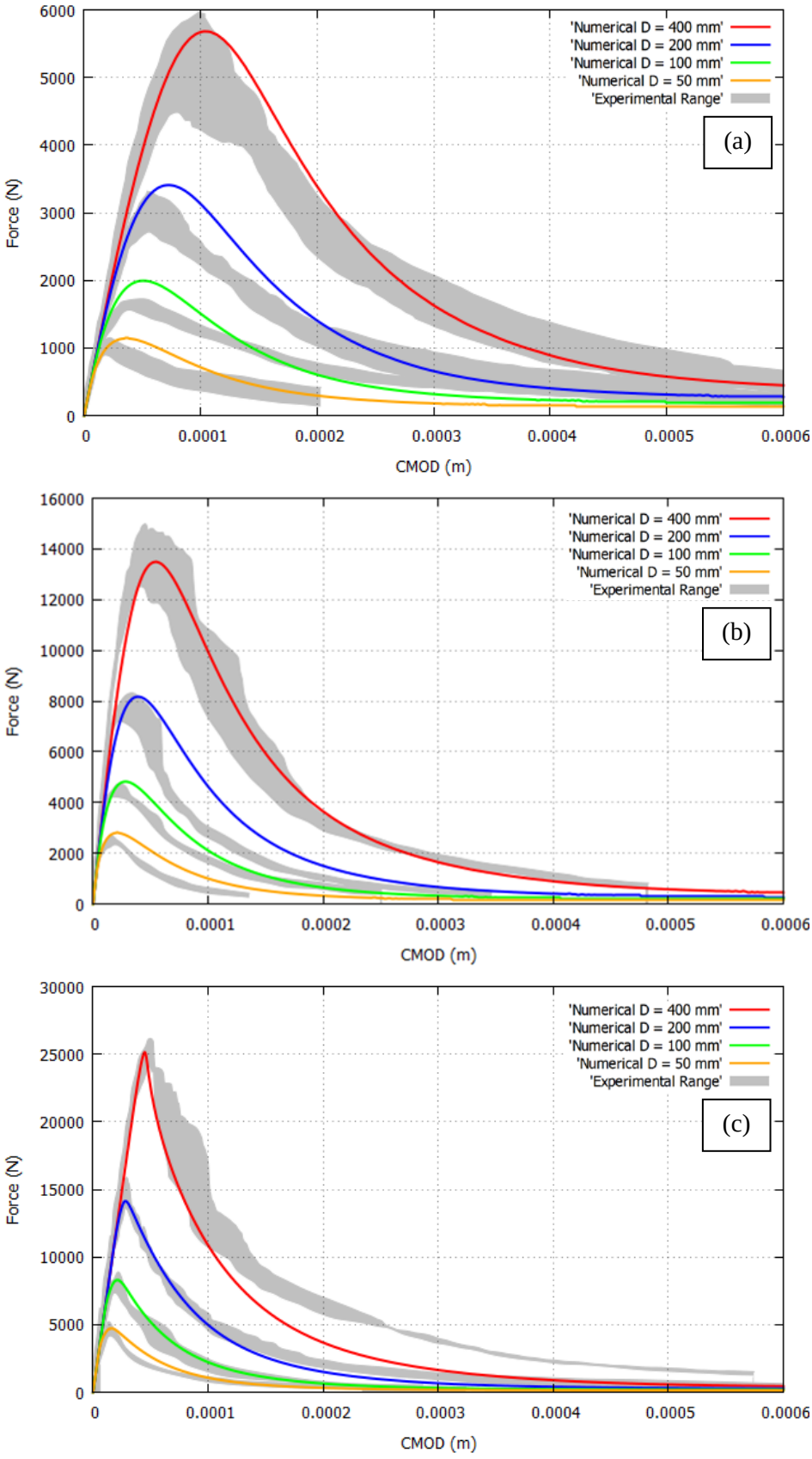

Figure 5. Force-CMOD curves of the Grégoire Tests for (a) the half-notched beams, (b) the fifth-notched beams and (c) the unnotched beams

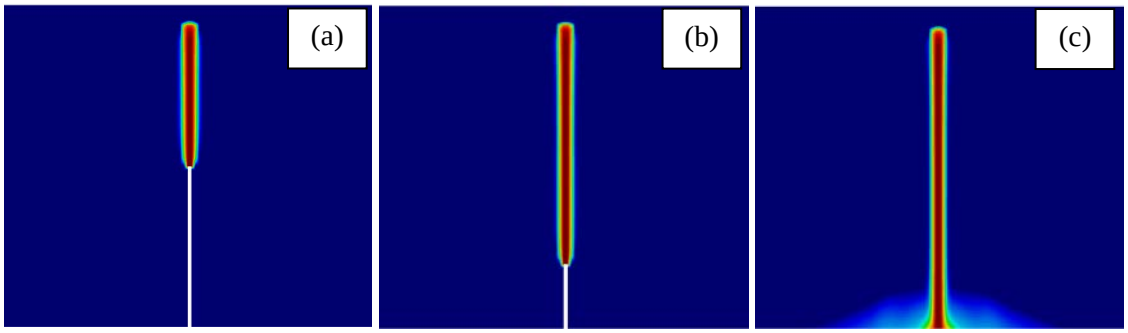

Figure 6. Damage contours of the Grégoire Tests in the 200 mm depth beams for (a) the half-notched case, (b) the fifth-notched case and (c) the unnotched case

Figure 6 shows the computed crack trajectories for the three different notch configurations of the beams with a depth of 200 mm. In all the beam sizes considered, the computed crack trajectory is a straight vertical line starting from the tip of the notch at the midpoint of the beam. For the unnotched series, an area of low value damage develops at the bottom midpoint of the beam prior to the strain localization.

5.2. Analysis of the Hoover tests: mode I fracture

In this second example, the numerical simulation of the beams of the Hoover experiments is considered. The tests are described in reference [44] and were repeated in reference [52]. Other numerical simulations of the tests can be found in references [25, 53, 54, 55, 56]. To perform their computations, reference [25] used a phase-field model, references [53] and [54] considered nonlocal models, reference [55] employed a cohesive crack model and reference [56] compared the performance between a nonlocal model and the XFEM approach.

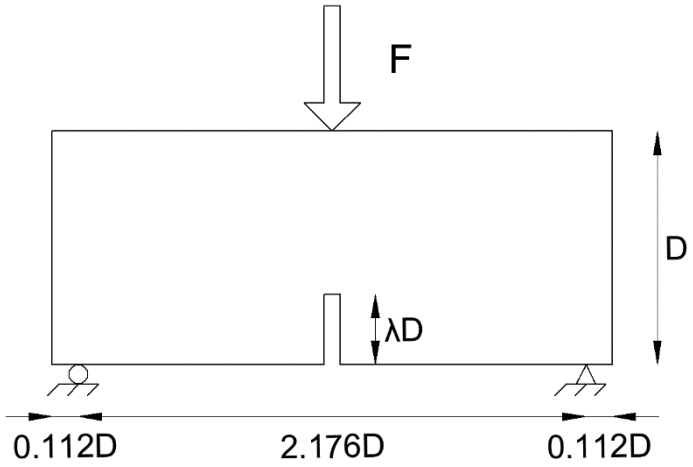

Figure 7. Geometry of the Hoover experimental tests

Young's Modulus	$41.0 \cdot 10^9$ Pa
Poisson's Ratio	0.17
Tensile Strength	$4.1 \cdot 10^6$ Pa
Tensile Fracture Energy	72.5 J/m^2
Irwin's material length	0.1768 m

Table 2. Material parameters of the Hoover tests

In the Hoover tests geometrically similar beams of varying sizes were subjected to three-point bending. The depths D of the tested units are 40 mm, 93 mm, 215 mm and 500 mm while the span-to-depth ratio was kept constant to 2.176. Five different notch-to-depth ratios λ were introduced: 0.3, 0.15, 0.075, 0.025 and 0.0 (unnotched). A constant thickness of 40 mm was kept for all the beam sizes. Details of the beam geometry are displayed in Figure 7. The beams are vertically loaded at the top midpoint. The simulations are done under CMOD control. Table 2 shows the material properties used for the Hoover tests. They are the same as the ones used for the numerical simulations reported in [25] and very close to the values recorded in the experiments.

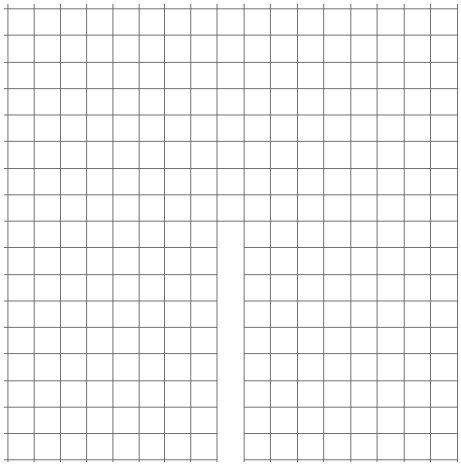

Figure 8. Detail of the mesh used for the Hoover tests around the tip of the notch

All the simulations are solved under the plane stress hypothesis using very similar structured meshes of 23970, 23985, 24092, 23898 and 23900 quadrilateral elements, depending on the notch configuration. The FE size is $10^{-2}D$, and the notch width is equal to the size of the element. In Figure 8, the detail of the mesh around the tip of the notch for the notch-to-depth ratio case of 0.3 is shown.

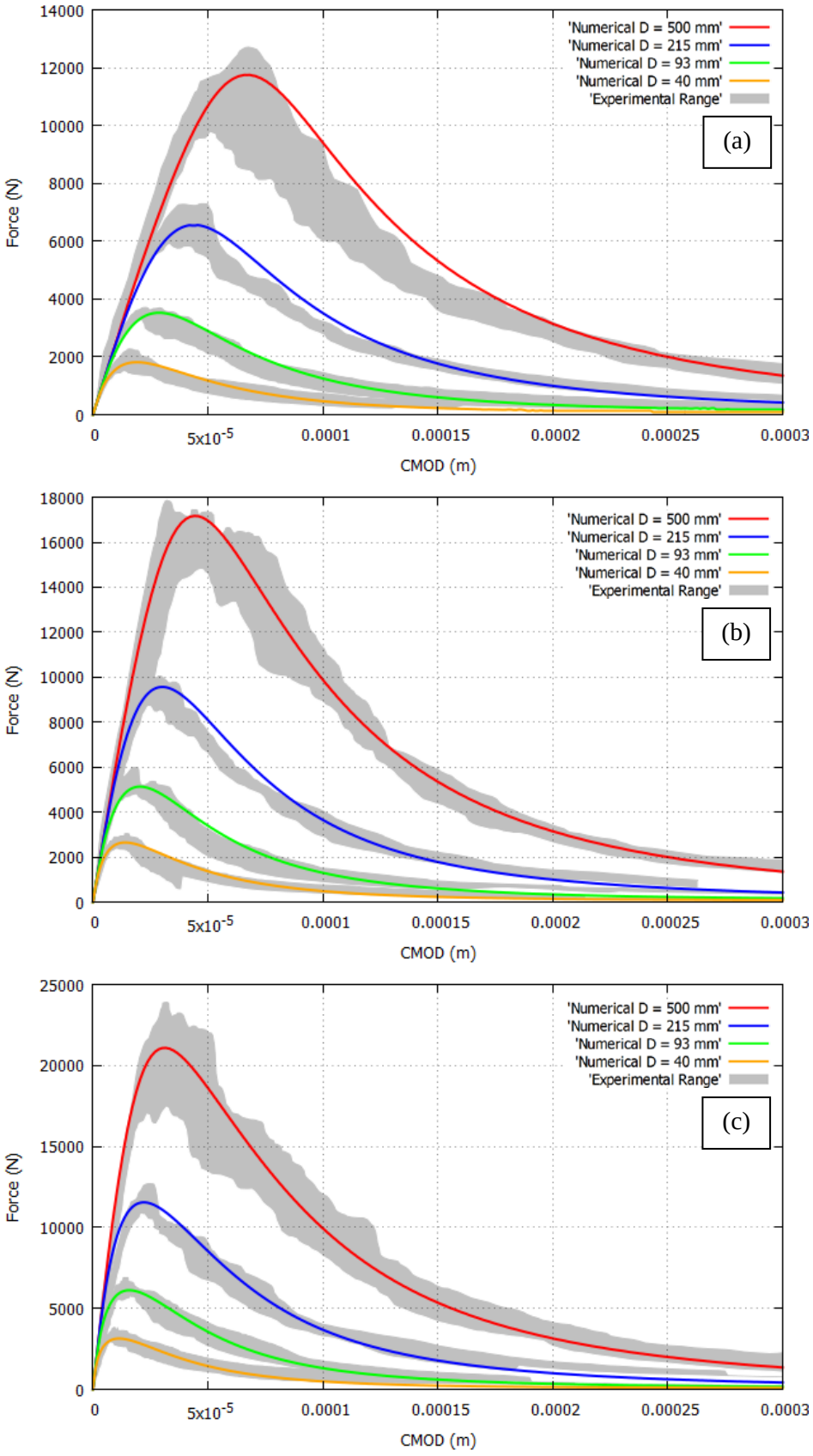

Figure 9. Force-CMOD curves of the Hoover Tests for notch to depth ratios of (a) 0.3, (b) 0.15 and (c) 0.075

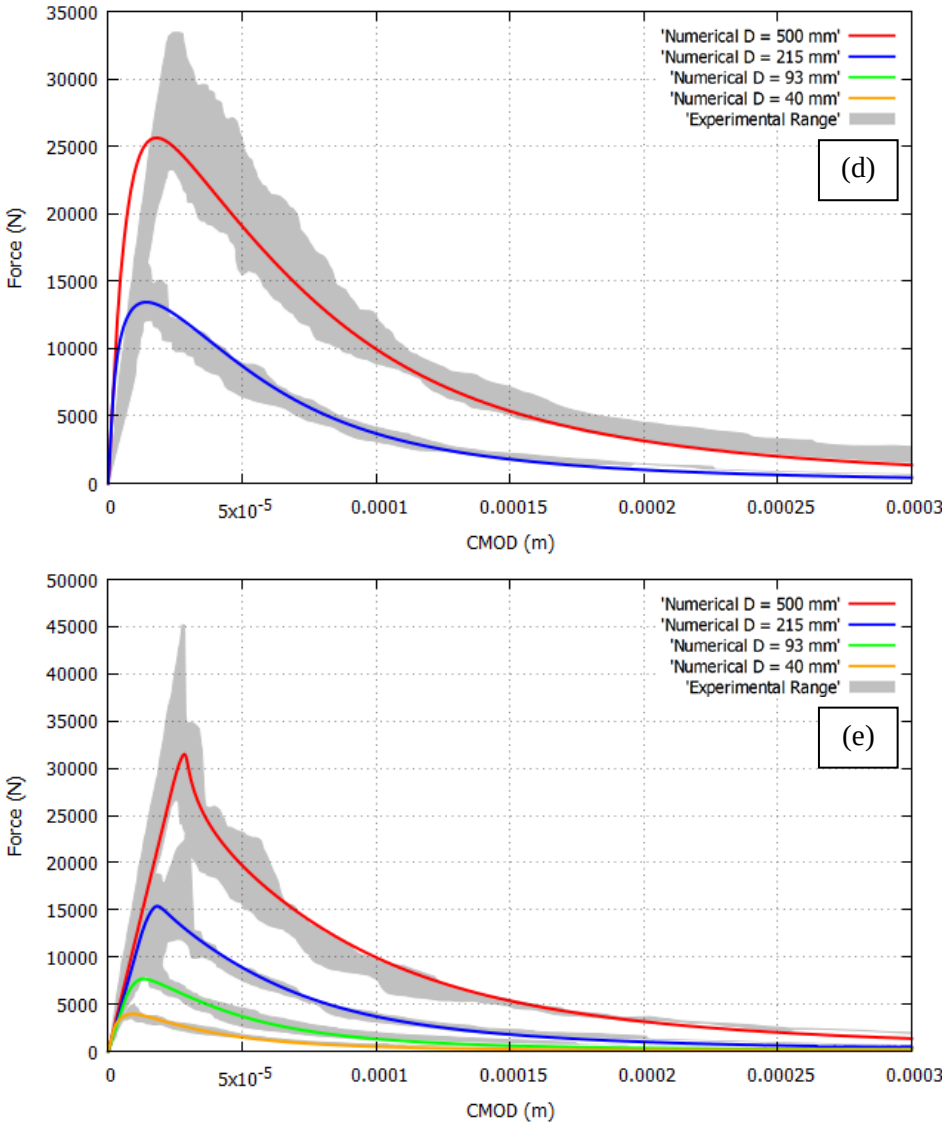

Figure 10. Force-CMOD curves of the Hoover Tests for notch to depth ratios of (d) 0.025 and (e) 0.0 (unnotched case)

Figure 9 and Figure 10 display the obtained force-CMOD curves. It is shown how the computed peak loads are inside the experimental range reported in [44] for all the sizes and all the notch configurations. Furthermore, the calculated post-peak softening behavior is also inside the experimental envelopes in practically all the situations. Again, the computational model is able to reproduce the size effect behavior observed in the experiments using the same set of material properties for all the sizes and beams with different notch-to-depth ratios.

Figure 11 depicts the computed damage contours of the 40 mm depth beams for the different notch-to-depth ratios considered in the tests. The computed track trajectories form a straight vertical line for all the beam sizes. Cracks initiate at the tip of the notch in the notched specimens. Like in the Grégoire tests, an area of low value of damage develops at the bottom midpoint of the unnotched specimens prior to the development of the vertical crack.

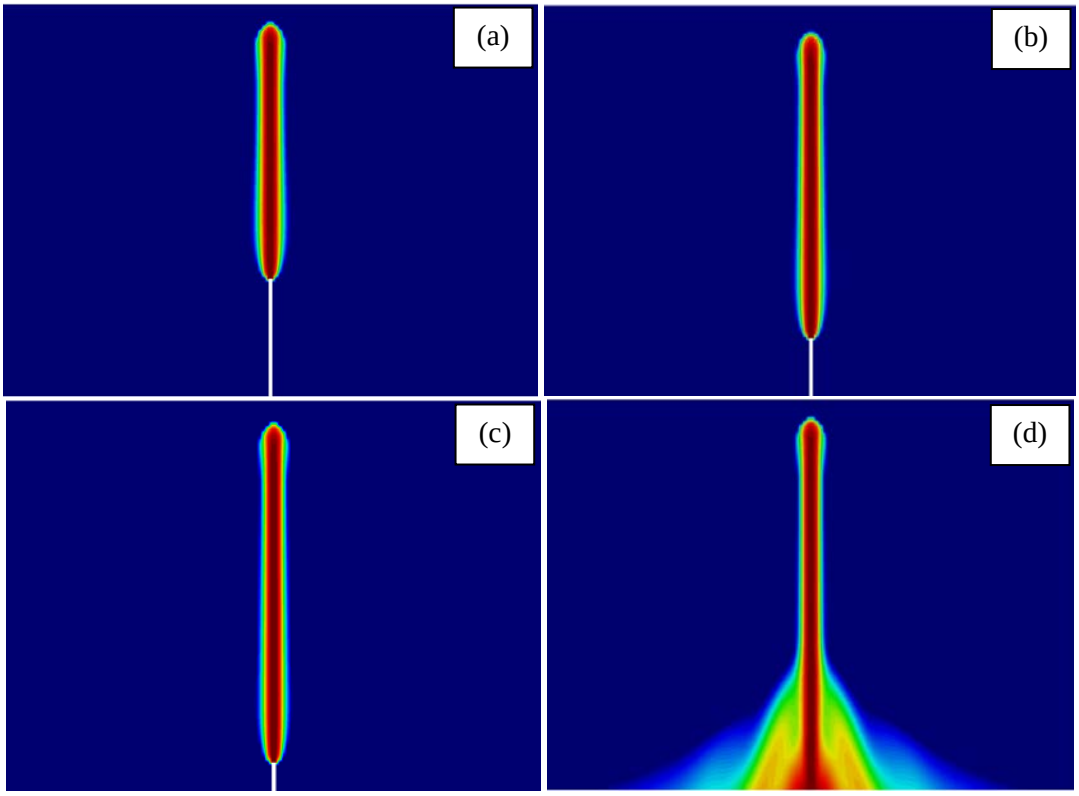

Figure 11. Damage contours of the Hoover Tests in the 40 mm depth beams for notch-to-depth ratios of (a) 0.3, (b) 0.15, (c) 0.075 and (d) 0.0 (unnotched case)

5.3. Analysis of the Garcia-Alvarez tests: mixed-mode fracture

In this section, the three-point bending tests performed by [45] are reproduced. In this case, an eccentricity of the notch was introduced in the beams, so that they are subjected to mixed-mode fracture. In [45] the experiments are also computationally modelled using interface elements. Other simulations of the results are reported in reference [25], where a phase-field approach is used.

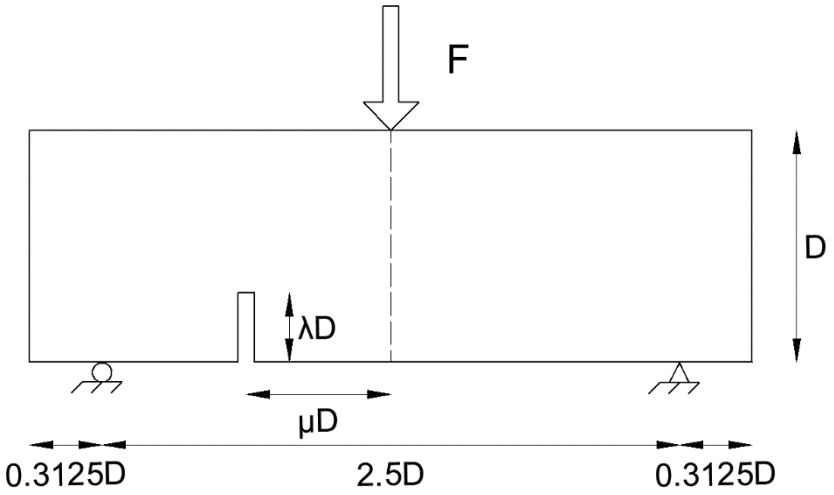

Figure 12. Geometry of the mixed-mode fractured beams

Young's Modulus	$33.8 \cdot 10^9$ Pa
Poisson's Ratio	0.2
Tensile Strength	$3.5 \cdot 10^6$ Pa
Tensile Fracture Energy	80 J/m^2
Irwin's material length	0.2207 m

Table 3. Material parameters for normal concrete strength in the mixed-mode fractured beams

Young's Modulus	$36.8 \cdot 10^9$ Pa
Poisson's Ratio	0.2
Tensile Strength	$6.0 \cdot 10^6$ Pa
Tensile Fracture Energy	120 J/m^2
Irwin's material length	0.1227 m

Table 4. Material parameters for high concrete strength in the mixed-mode fractured beams

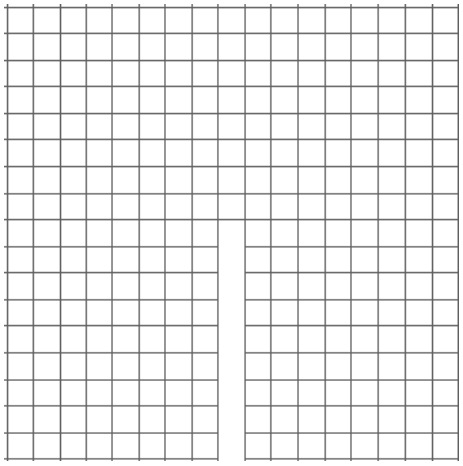

Figure 13. Detail of the mesh used for Garcia-Alvarez the mixed-mode fractured beams around the tip of the notch

Geometrically similar beams of depths D equal to 80 mm, 160 mm and 320 mm were tested while the span-to-depth ratio was kept constant to 2.5. Three different series were considered, where different notch eccentricities μD of $0.625D$, $0.3125D$ and $0.0D$ were introduced. The notch-to-depth ratio λ is 0.25 in all beams. The thickness of all the beams is 50 mm. The details of the geometry of the beams are shown in Figure 12. The material properties used in the present work are shown in Table 3. They are identical to the ones reported in [45] as well as the ones used in the corresponding numerical simulations in [25]. A vertical force is applied at the top midpoint of all the beams. The numerical simulations are performed under CMOD control.

In addition, a supplementary series of experiments is reported in [45], where high strength concrete was employed, instead of normal strength concrete. The beam depths were again 80 mm, 160 mm and 320 mm. In this case, no eccentricity was considered ($\mu = 0.0$) and the notch-to-depth ratio λ was 0.275. The material properties used to simulate the high concrete strength case, which are again the same as the ones reported in [45], are shown in Table 4.

All the simulations are solved under the plane stress hypothesis using very similar structured meshes of approximately 31000 quadrilateral elements, depending on the notch configuration. The size of the finite elements is $10^{-2} \cdot D$ and the width of the notch is set equal to the element size. In Figure 13, the detail around the tip of the notch of the mesh used for the case with an eccentricity of $0.625D$ is shown.

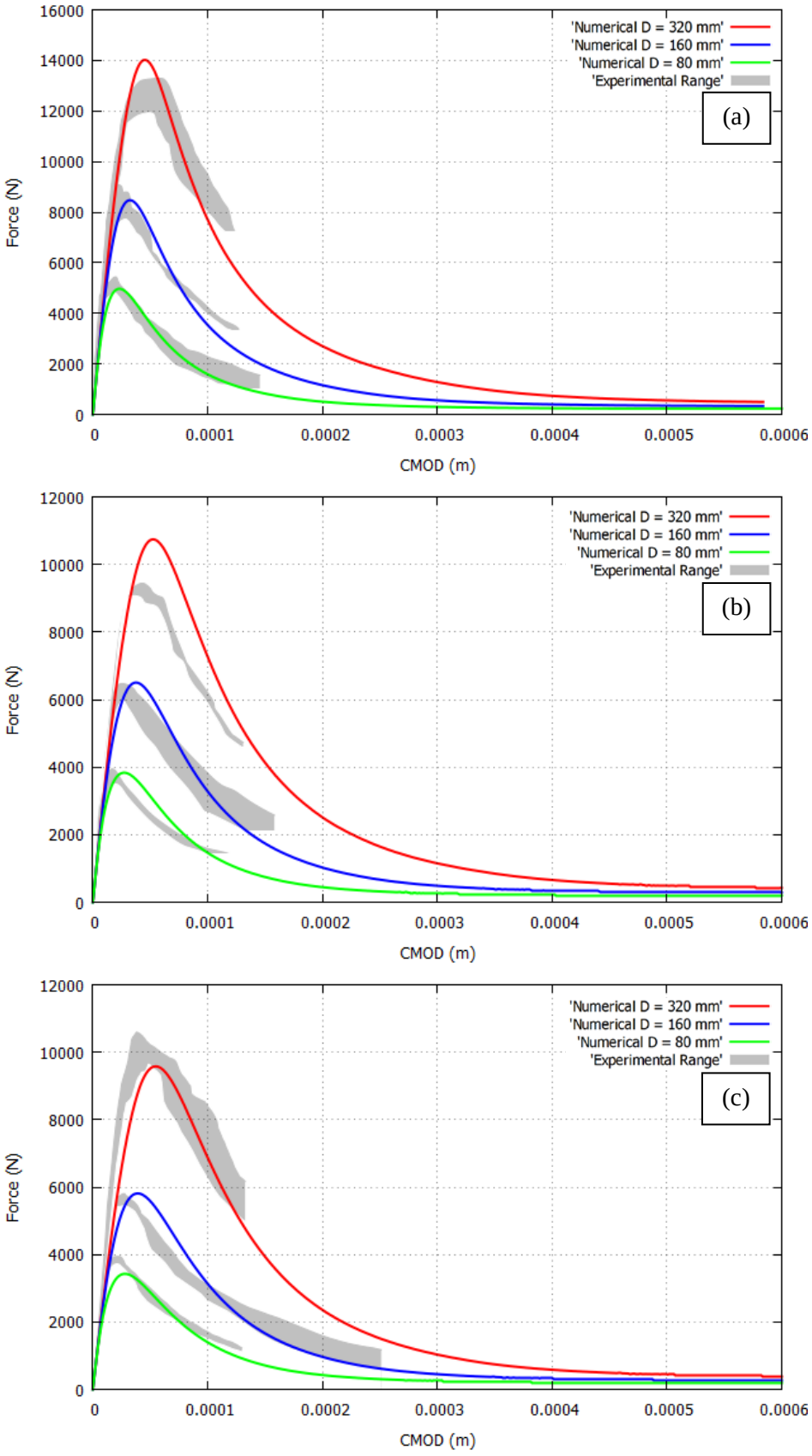

Figure 14. Force-CMOD curves of the mixed-mode fractured beams for the normal concrete strength specimens with eccentricities of (a) 0.625*D*, (b) 0.3125*D* and (c) 0.0*D*

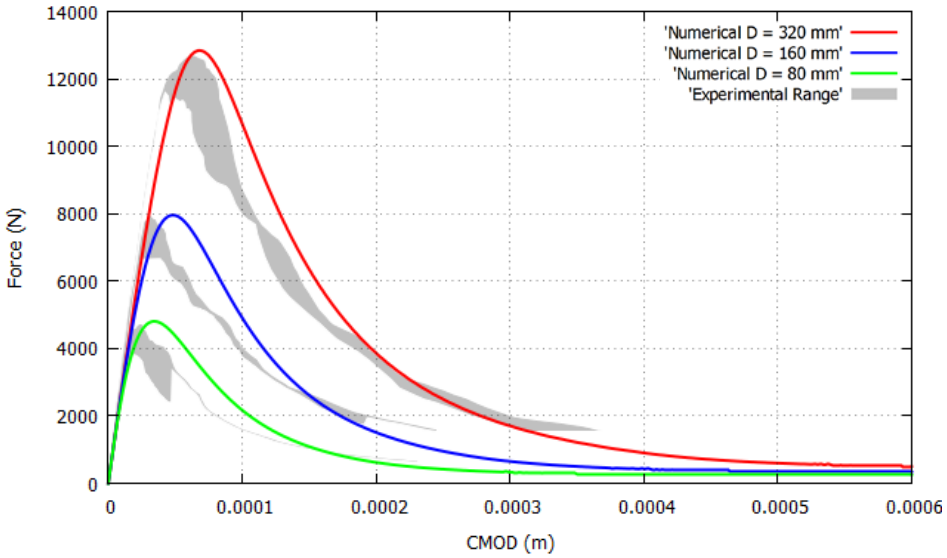

Figure 15. Force-CMOD curves of the mixed-mode fractured beams for the high concrete strength specimens

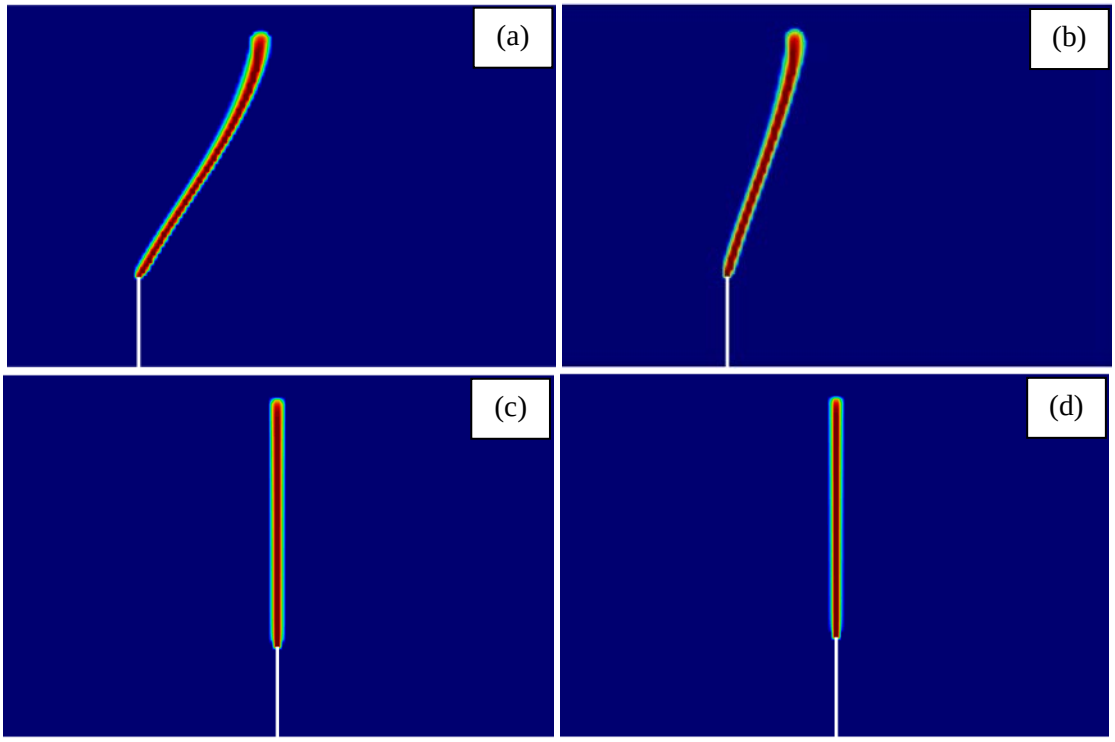

Figure 16. Damage contours of the mixed-mode fractured beams in the 320 mm depth case for the normal concrete strength specimens with eccentricities (a) 0.625*D*, (b) 0.3125*D* and (c) 0.0*D* and for (d) the high concrete strength specimens

Figure 14 and Figure 15 show the force-CMOD curves obtained for the normal and high concrete specimens. Once more it can be seen that the results in terms of peak loads and post-peak softening curves are very similar to the experiments in all the cases. The agreement with the limited data documented from the tests is notable. The same set of material properties produce very reasonable simulations of the force-CMOD curves when compared with the narrow experimental range provided.

Figure 16 depicts the damage contours computed in the 320 mm depth beams for the different eccentricities contemplated in the tests for normal and high strength concretes. The cases with no eccentricity produce a vertical straight line for all the sizes. In the specimens with eccentricity the crack trajectories start at the tip of the notch and deviate towards the center of the beam where the vertical load is applied.

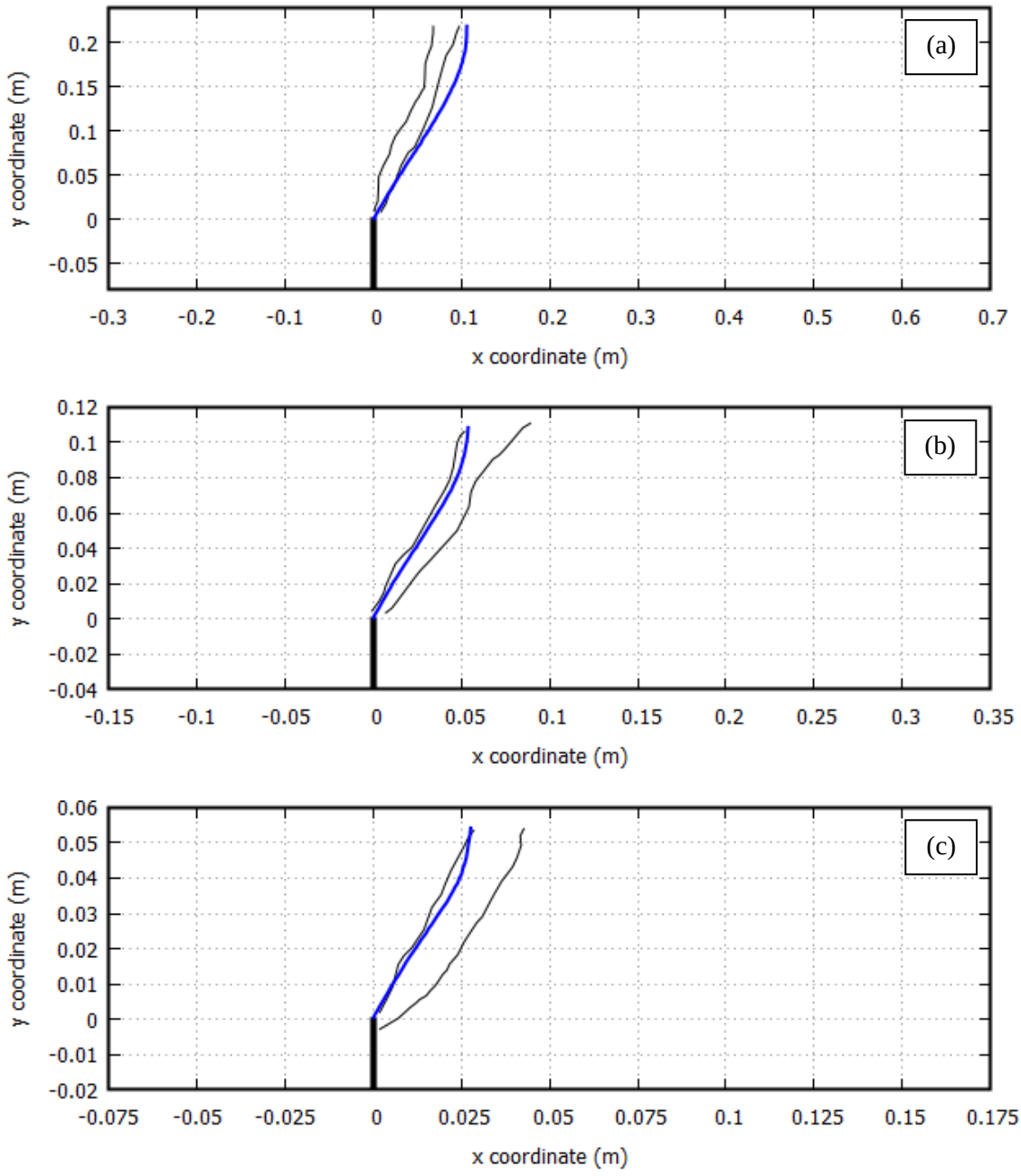

Figure 17. Computed crack paths compared to the experimental results of the mixed-mode fractured beams with a notch eccentricity of 0.625*D* for depths (a) 320 mm, (b) 160 mm and (c) 80 mm

The computed crack trajectories of the beams with eccentricities 0.625*D* and 0.3125*D* are compared in detail for all the sizes with the experimental results in Figure 17 and Figure 18, respectively. It can be seen that the computed crack paths show very good agreement with the test results. In all the cases except the first one the crack is inside the experimental range. The overall behavior of the model is considered very satisfactory given the limited data of the

experiments provided and the simplicity of the material model considered, an isotropic damage model. The Drucker-Prager criterion is more suitable for mixed-mode cracking, as shown in reference [30]. However, for the numerical simulations of these experiments, the Rankine damage model produces satisfactory results in terms of crack trajectories and force-displacement curves when compared to the test results and is able to properly capture the observed size effect phenomenon.

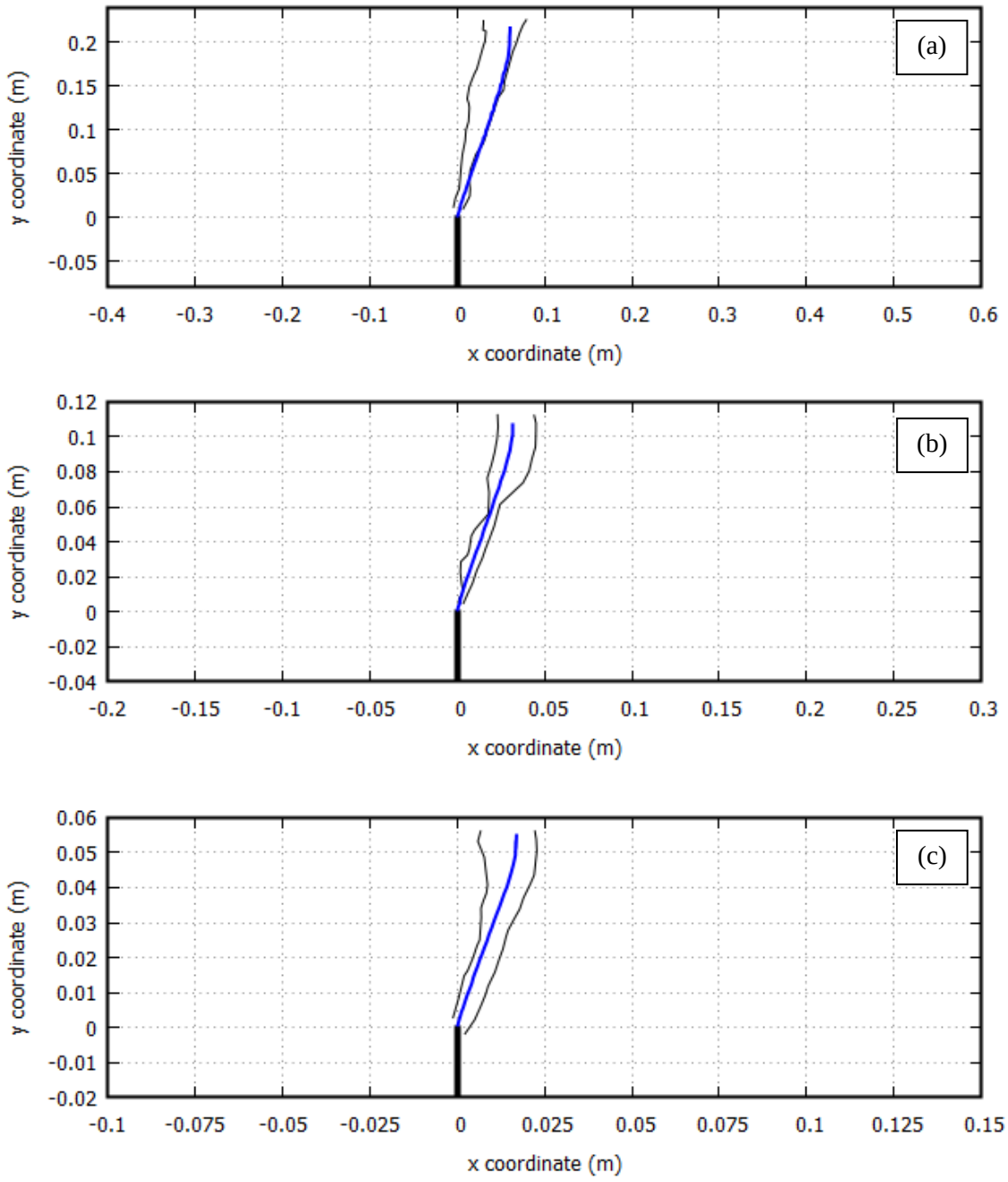

Figure 18. Computed crack paths compared to the experimental results of the mixed-mode fractured beams with a notch eccentricity of 0.3125*D* for depths (a) 320 mm, (b) 160 mm and (c) 80 mm

6. Mesh dependence study

In this section the performance of the mixed FE formulation is assessed. The sensitivity of the computed results with regard to the mesh used is analyzed. First, a comparison between 2D and 3D computations is considered. Then, solutions obtained with different mesh sizes and orientations are also contrasted. At the end of this section, a mesh independence study is also carried out comparing with standard irreducible linear and quadratic FE.

6.1. 2D vs 3D simulations

In this section, the computed results obtained in 2D for the mixed-mode fractured beams in Section 5.3 are compared with corresponding 3D simulations. Specifically, the series with a notch eccentricity of $0.625D$ is taken into account for this study. The objective of this section is to show the capacity of the proposed model to accurately simulate the experiments in 3D and, reciprocally, to assess the plane stress hypothesis commonly used in beam analysis. The material properties of the simulation are the same as those used in 2D, shown in Table 3. The simulations of this section are performed with a mesh of 18475 hexahedral elements. The size of the FEs in the mesh used is $10^{-2}D$ in the central part where the crack forms and of $3.125 \cdot 10^{-2}D$ in the rest of the beam. The notch width is also equal to $10^{-2}D$.

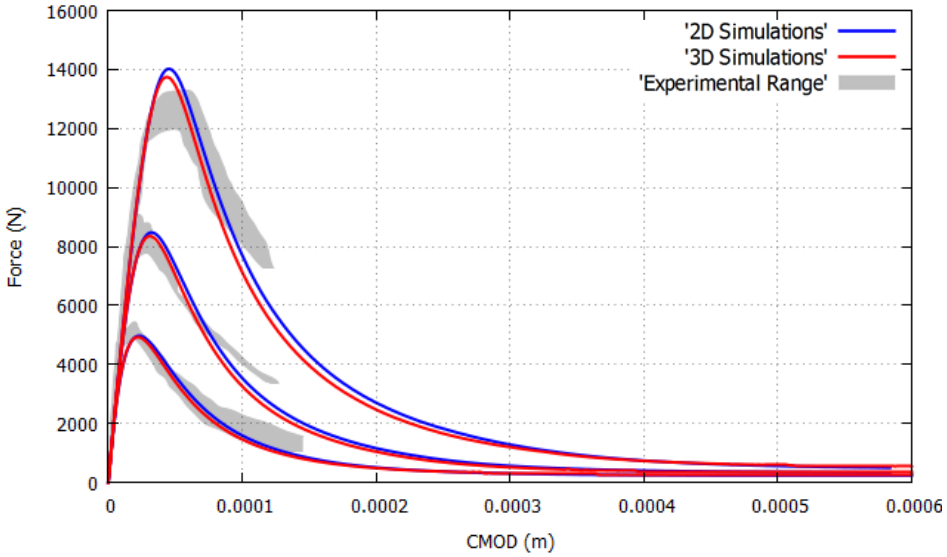

Figure 19. Force-CMOD curves of the mixed-mode fractured beams for the specimens with eccentricities of $0.625D$, in 2D and 3D

In the computed force-CMOD curves shown in Figure 19 the 2D and 3D results are almost overlapping and very close to the experimental range for all the sizes. The 2D numerical simulations produce a slightly larger peak load than in 3D. Force-displacement curves computed in 2D under the plane stress hypothesis are typically an upper bound to 3D results. The small difference is due to the disregardance of the out-of-plane stress components in the 2D simulation. In addition, the computed crack paths displayed in Figure 20 also show almost identical results and with good agreement with the test data. The crack surfaces obtained in the 3D analyses are depicted in Figure 21, showing the capacity of the model to accurately compute the 3D fracture surfaces that occur under mixed-mode fracture. This confirms that the plane stress hypothesis used to compute the results in 2D is appropriate for simulating the beam experiments.

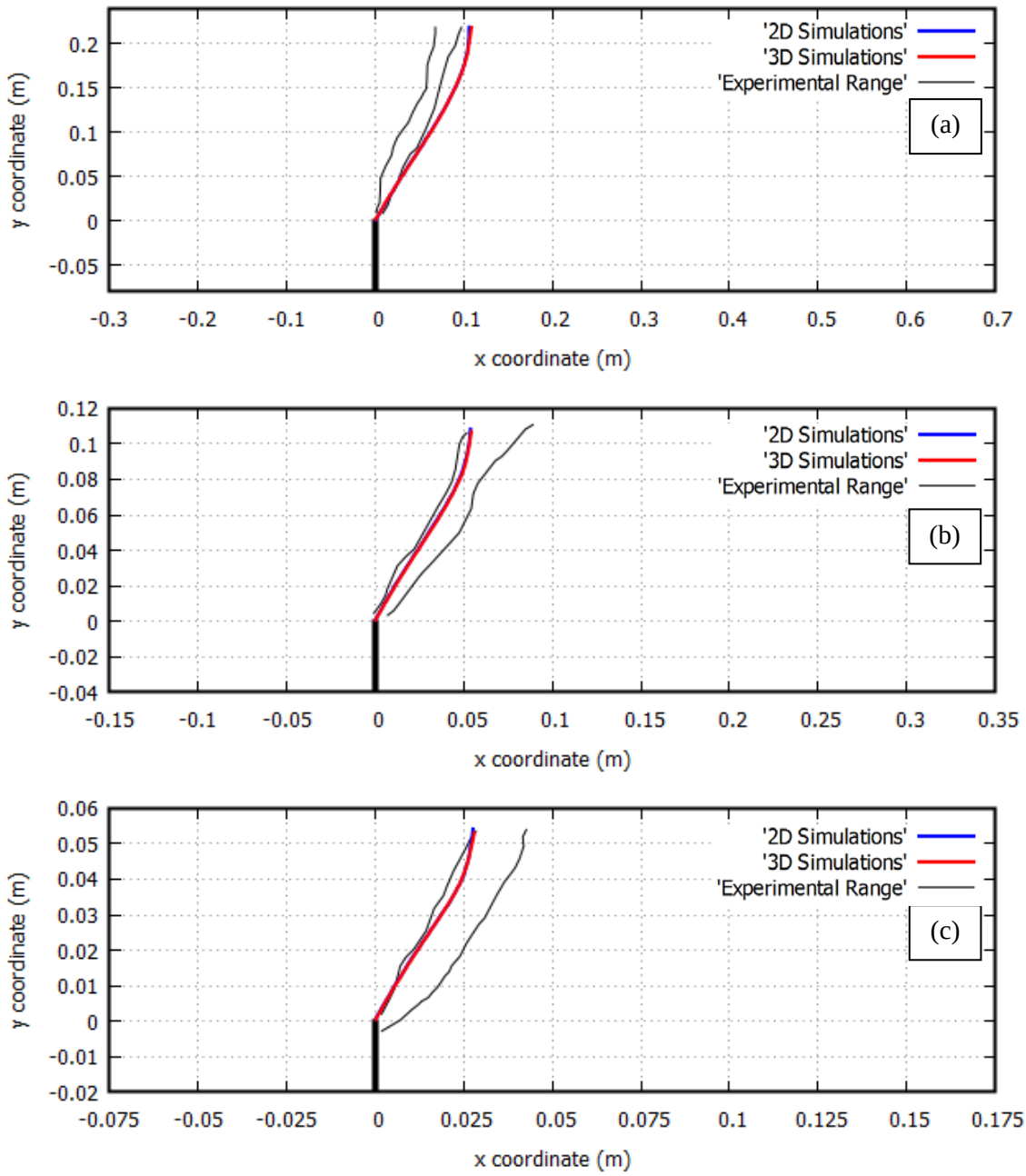

Figure 20. Computed crack paths in 2D and 3D of the mixed-mode fractured beams with a notch eccentricity of 0.625*D* for depths (a) 320 mm, (b) 160 mm and (c) 80 mm

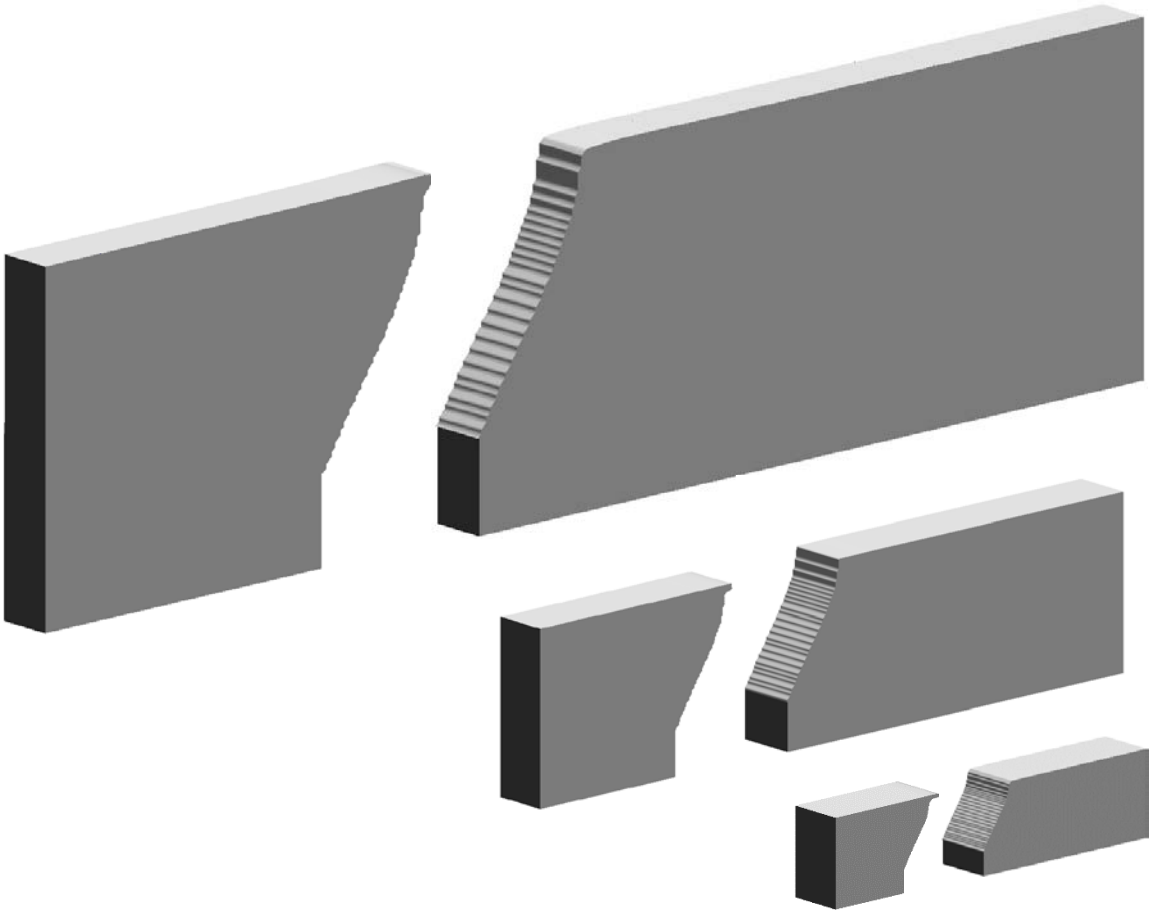

Figure 21. Computed crack surfaces of the mixed-mode fractured beams with eccentricity 0.625*D* for the three sizes of the series

6.2. Mesh independence study with mixed FE

The objective of the present section is to assess the capability of the mixed FE formulation of obtaining mesh-objective results with regard FE size and orientation. For this, the computation of the specimen with depth D of 80 mm and a notch eccentricity of 0.3125D of the mixed mode fracture tests reported in Section 5.3 is considered. Four different meshes are used for this study: (1) a 31175 quadrilateral element structured mesh already used in Section 5.3, (2) a 64700 quadrilateral element structured mesh, (3) a 36714 triangular element unstructured mesh and (4) a 126530 triangular element unstructured mesh. Meshes (1) and (3) have a FE size corresponding to $10^{-2}D$ in the center of the beam while in (2) and (4) the FE size is equal to $5 \cdot 10^{-3}D$ in the center of the beam. In all the cases, the width of the notch is equivalent to $10^{-2}D$. Different element orientations have been chosen for the triangular and quadrilateral meshes to test the mesh size and bias dependence of the computed results, as it can be seen in Figure 22.

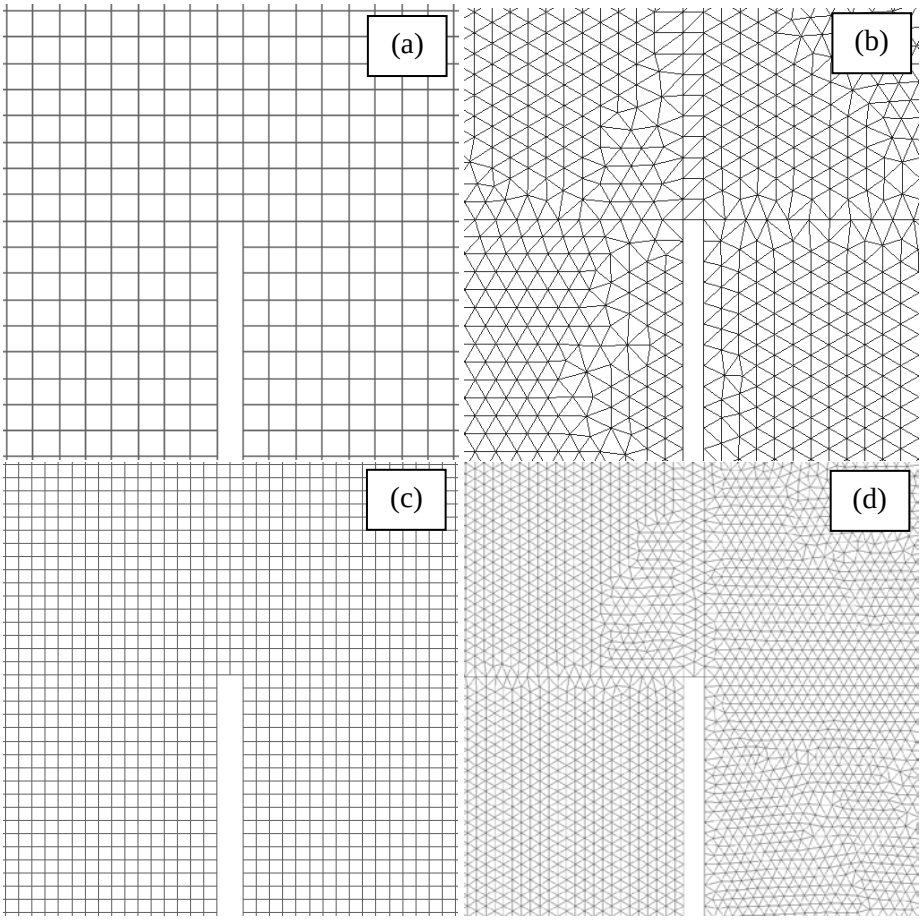

Figure 22. Detail of the mesh around the notch tip used for the mixed-mode fractured beams with (a) 31175 quadrilateral elements, (b) 36714 triangular elements, (c) 64700 quadrilateral elements and (d) 126530 triangular elements

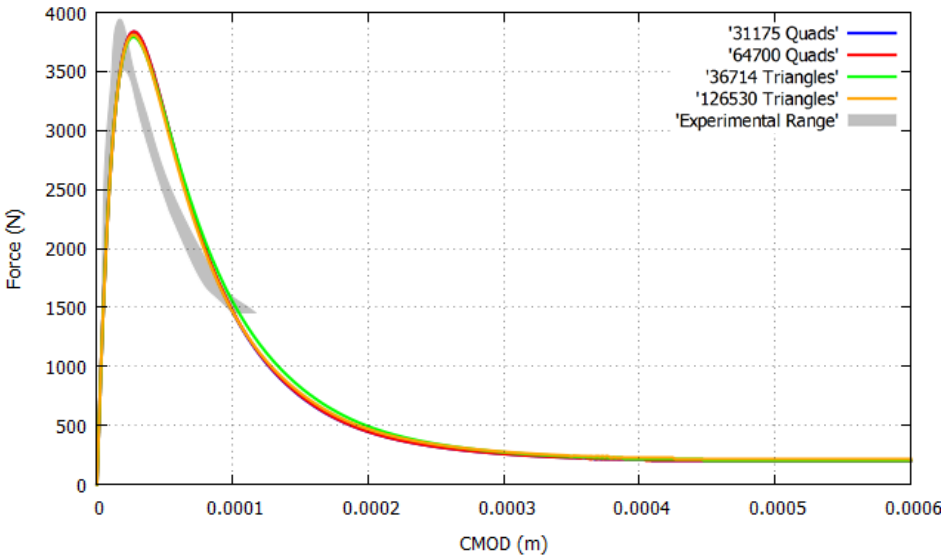

Figure 23. Force-CMOD curves of the mixed-mode fractured beams for the 80 mm depth specimen with 0.3125*D* eccentricity for the different meshes considered

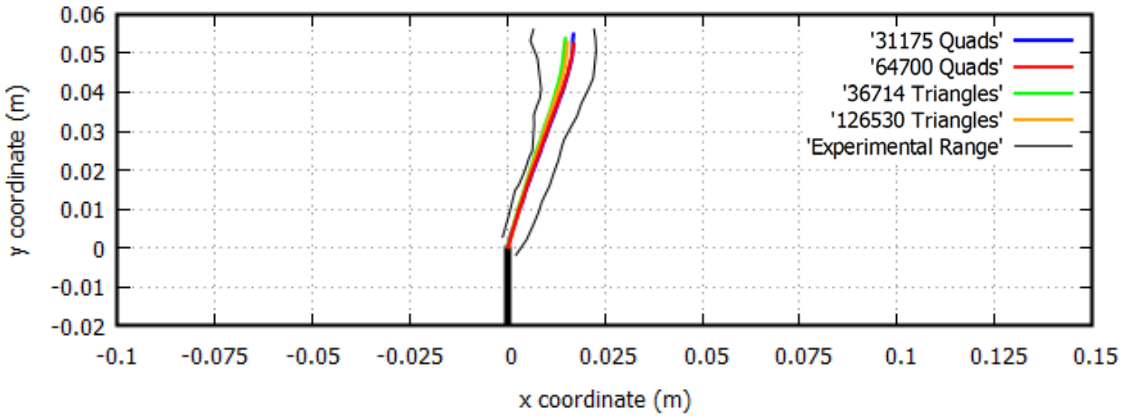

Figure 24. Computed crack paths of the mixed-mode fractured beams for the 80 mm depth specimen with 0.3125*D* eccentricity for the different meshes considered

Figure 23 shows the force-CMOD results obtained with the 4 different meshes. It can be seen that the results for all the meshes are almost overlapping and very close to the experimental result. The computed crack paths for the 4 meshes are depicted in Figure 24. They are all of them almost identical, the difference between each other being of the order of the FE size h.

Therefore, it can be concluded that: (1) the computed results are converged in terms of mesh size, (2) the mixed finite element formulation used is practically mesh-independent and does not show any spurious mesh-orientation bias.

6.3. Standard vs Mixed FE

In this section a comparison of the performance of standard and mixed FE is carried out. For this, the numerical simulation of the specimen with depth D of 80 mm and a notch eccentricity of $0.3125D$ of the mixed mode fracture tests of Section 5.3 is considered again. The computations using standard and mixed FE are compared for two different meshes: (1) the 31175 quadrilateral element mesh shown in Figure 22a and (2) the 36714 triangular element mesh depicted in Figure 22b.

In Figure 25 it can be seen that the force-CMOD computations for the standard and mixed FE are very close. This is significant because, as shown in Figure 26, the computed crack trajectories of the standard FE are completely off-mark, demonstrating the spurious mesh bias of this element while the paths obtained with mixed FE are inside the experimental range.

Finally, 3D simulations have been performed to further illustrate the spurious mesh dependence of standard FE. For this, considering the same specimen, an 18475 hexahedral element mesh has been used to assess the performance of standard tri-linear elements, standard tri-quadratic and mixed tri-linear FE. The size of the mesh is $10^{-2}D$ in the central part where the crack forms and of $3.125 \cdot 10^{-2}D$ in the rest of the beam. The notch width is also equal to $10^{-2}D$.

Figure 27 depicts the computed crack paths of the three simulations. On the one hand, it can be seen again how the linear standard formulation produces severely mesh dependent results. The results obtained with quadratic standard elements are closer to experimental range than the ones obtained with linear standard FE, but it is clearly visible that they suffer from spurious mesh dependence. On the other hand, the results computed with mixed FE are inside the experimental range. This can be seen in detail in Figure 28, where the computed 3D crack surfaces with the three elements are shown.

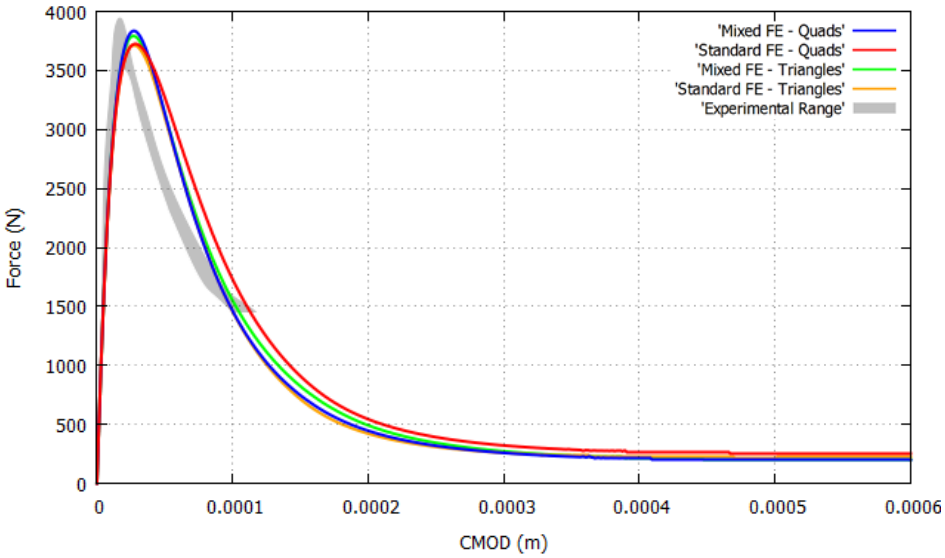

Figure 25. Force-CMOD curves of the mixed-mode fractured beams for the 80 mm depth specimen with 0.3125*D* eccentricity for standard and mixed FE

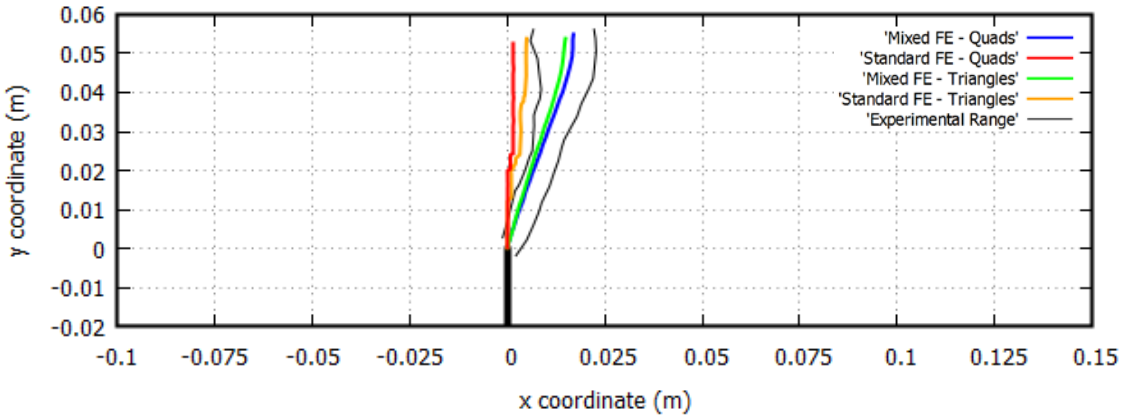

Figure 26. Computed crack paths of the mixed-mode fractured beams for the 80 mm depth specimen with 0.3125*D* eccentricity for standard and mixed FE

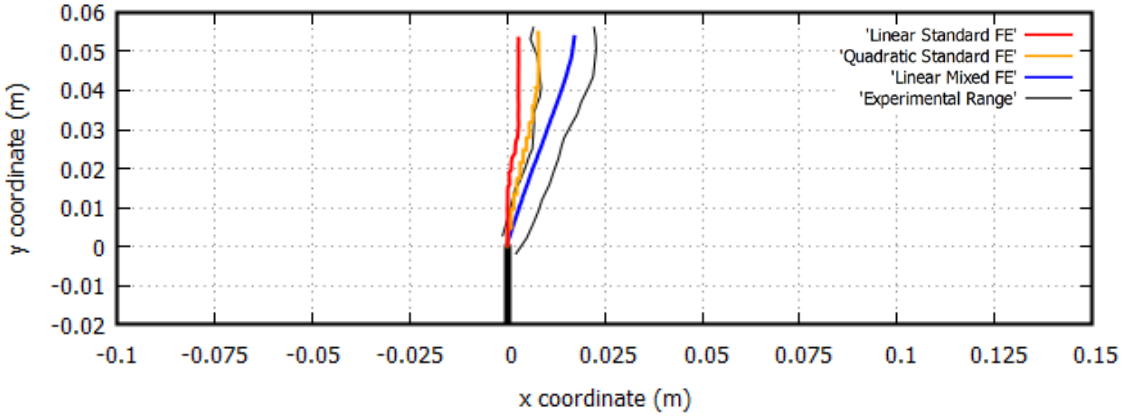

Figure 27. Computed crack paths of the mixed-mode fractured beams for the 80 mm depth specimen with 0.3125*D* eccentricity in 3D for standard and mixed FE

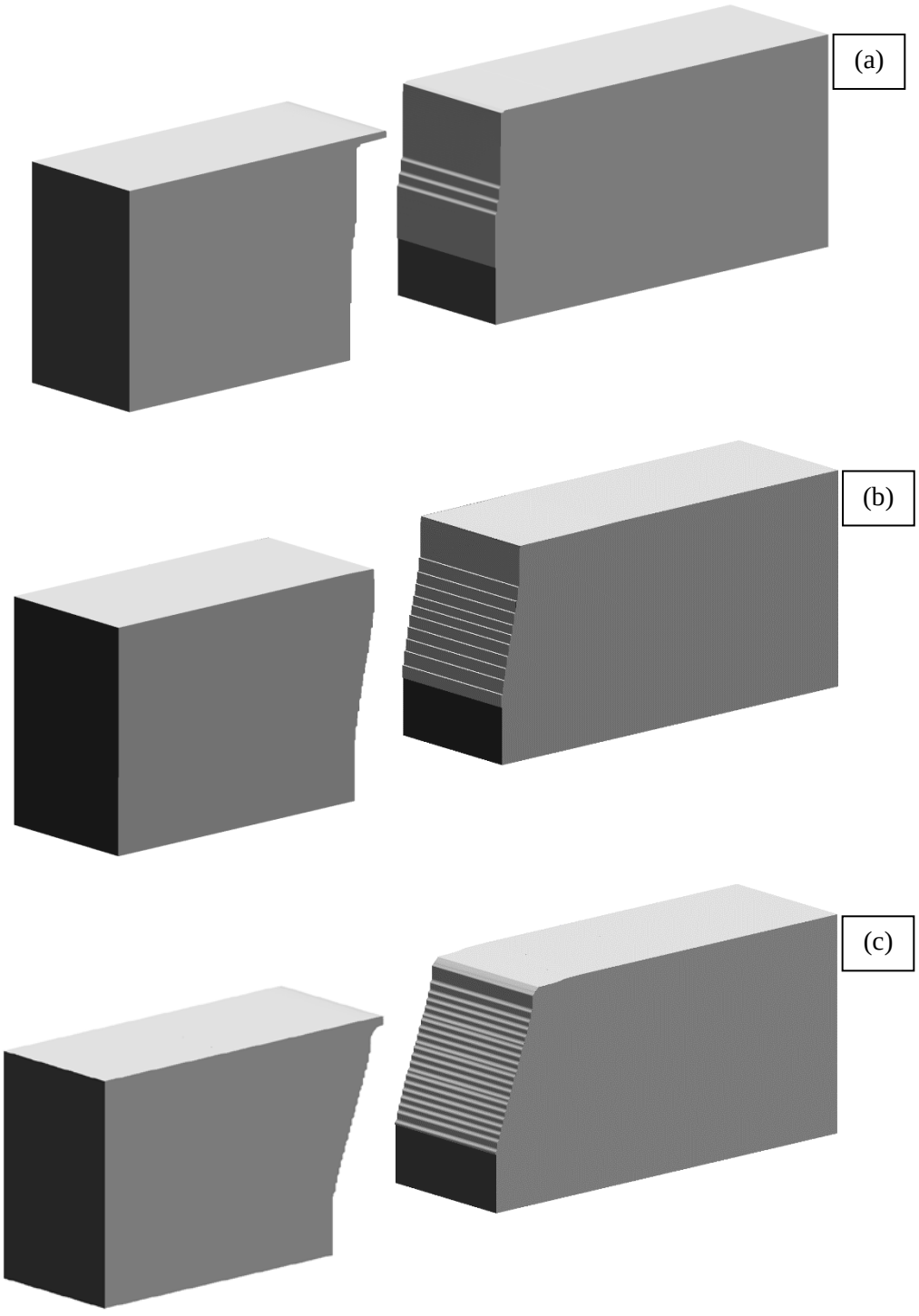

Figure 28. Computed crack surfaces of the mixed-mode fractured beams for the 80 mm depth specimen with 0.3125*D* eccentricity with (a) linear standard FE, (b) quadratic standard FE and (c) linear mixed FE

7. **Influence of the statistical variability of the mechanical properties**

The objective of this section is to analyse the influence of the statistical size effect compared to the impact that the release of stored energy has on the size effect phenomenon. It has been stated by Bazant and Planas in reference [1] that

> "*Statistical size effect … is caused by the randomness of material strength and has traditionally been believed to explain most size effects in concrete structures. … However, … on closer scrutiny, this explanation is found to be inapplicable to most types of failures of reinforced concrete structures. … Concrete structures fail only after a large stable growth of cracking zones or fractures. The stable crack growth causes large stress redistributions and a release of stored energy, which, in turn, causes a much stronger size effect, dominating over any possible statistical size effect. At the same time, the mechanics of failure restricts the possible locations of the decisive crack growth at the moment of failure to a very small zone. This causes the random strength values outside this zone to become irrelevant, thus suppressing the statistical size effect.* "

In the analysis of this section the beams of the Hoover series corresponding to the notch-to-depth ratio of 0.075 are computed considering the statistical variability of the mechanical properties of the material that was reported in [44, 52]. In the present study, only the variability of the Young modulus E, the tensile strength f_t and the fracture energy G_f are considered, as they are deemed to be the most influential in the structural response.

CV Young's Modulus	5%
CV Tensile Strength	3.5%
CV Tensile Fracture Energy	17%

Table 5. Coefficients of variation of the material parameters adopted for the Hoover tests

An accurate study of the relative influence of the deterministic and stochastic sources of size effect in quasi-brittle materials would necessarily include a certain number of numerical simulations where different material properties are randomly assigned to each finite element according to a probability density function and a spatial autocorrelation function.

R	Young's Modulus ($x10^{10}$ Pa)	Tensile Strength ($x10^{6}$ Pa)	Tensile Fracture Energy (J/m2)
1	4.1647	3.9172	68.219
2	4.2129	4.3060	77.698
3	3.8494	4.3789	88.638
4	4.3171	4.0705	75.954
5	4.1522	4.0352	84.161
6	3.9682	4.2678	56.885
7	4.4500	4.1607	82.345
8	4.0652	4.0529	58.623
9	3.7394	4.0908	81.015

Table 6. Sets of random properties generated for the Hoover tests

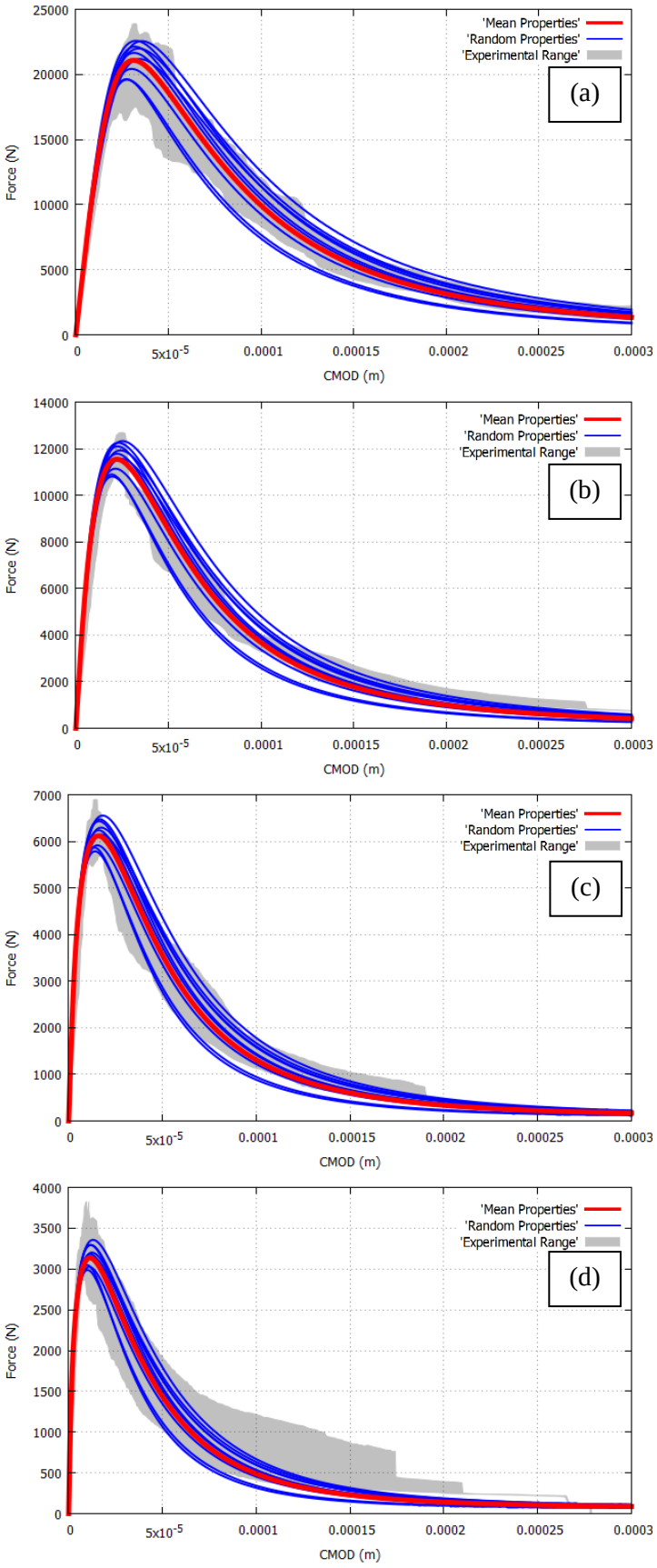

Figure 29. Force-CMOD curves of the Hoover Tests with the random properties generated, notch-to-depth ratio 0.075, for depths (a) 500 mm, (b) 215 mm, (c) 93 mm and (d) 40 mm

This process is here circumvented on the consideration that, even when the variability of the material is taken into account with the aforementioned method, for large enough specimens of quasi-brittle materials the crack is going to localize through a band of elements which represents a small percentage of the total number of elements. The behavior of the whole specimen is going to be determined by the material parameters of the very few elements located at the crack path. When considering as well the spatial correlation of the material properties, an effective and simpler way to tackle the issue is to assign to the whole body the same equivalent set of random parameters generated according to a certain probability density function.

Of course it is necessary to keep in mind the limitations of the present simplified approach to statistical size effect. On the one hand, in reference [57] it is shown that for small enough specimens, where the previous considerations are no longer acceptable, the influence of statistical size effect increases significantly. To consider that case, performing the simulations with varying properties in each element is mandatory. On the other hand, reference [33] states that for very large unnotched structures, where a very brittle failure takes place as soon as the fracture process starts, statistical size effect also becomes significant. However, for the sizes used in the Hoover tests the present simplified approach is deemed accurate enough.

For the computations of this section, it is assumed that the three material properties considered follow a Gaussian distribution. The mean values of the three properties are taken as the ones already used in the simulations of the present work in Table 2. The coefficients of variation adopted in this work (displayed in Table 5) are the ones reported in [44, 52]. With this data, 9 different sets of properties have been randomly generated, noted R1 to R9 and are shown in Table 6. These properties are used to simulate the four sizes of the Hoover beam series with a notch-to-depth ratio of 0.075.

The computed force-CMOD curves are shown in Figure 29. It can be seen how all the different randomly generated sets of properties produce results with good agreement with the experiments for all the sizes. In all the cases the values of the peak loads are inside the experimental range. The post-peak softening numerical result is very similar to the behavior observed in the tests. The ranges of numerical results generated overlap quite satisfactorily with the experimental envelopes. In this case the impact of statistical size effect is small and the size effect phenomenon can be sufficiently reproduced considering only the influence of the release of stored energy.

8. **Size effect law predictions**

It has been shown so far that the proposed model based on the mixed finite element formulation together with the proper constitutive law is able to reproduce with accuracy the size effect phenomena observed in experiments. The objective of this section is to perform a comprehensive analysis of the size effect phenomenon. For this, numerical simulations have been carried out for an extended range of sizes in notched and unnotched beams. The aptness of the model in reproducing the behavior theoretically expected is assessed in detail.

The Grégoire tests are considered for computing predictions of the behavior of notched and unnotched beams over a large interval of sizes. Specifically, the Grégoire series with a notch-to-depth ratio of 0.2 and 0.0 are contemplated. When taking the case with depth 400 mm as reference, computations with geometries scaled up to 10^2 times (and even more for the notched specimen) and 10^{-4} times smaller have been performed. In all the cases the same material properties from Table 1 are used and the thickness of the beam is kept constant to 50 mm.

Given the extensive range of sizes considered, there are several obvious factors that may alter the outcome of the extremely large and small tests that are not taken into consideration in the

simulations performed in this section. In particular, the impact of the other sources of size effect might increase. Considering the practical impossibility of performing the really big and really small scale tests in laboratory, the corresponding simulations presented are to be seen as a study of the limit cases for size effect.

In this section, the nominal strength σ_{N_u}, or peak nominal stress, is defined as

$$\sigma_{N_u} = \frac{P_u}{Db} \tag{26}$$

where P_u is the peak load, D is the depth of the beam and b is the thickness.

Unnotched beam size effect predictions

In Figure 30, the damage and maximum principal strain contour fills computed for a few cases are shown to demonstrate the change in the failure mode that happens when the size of the unnotched beam varies. The same mesh as the one used in the simulations of Section 5.1 is employed for all the scales. It can be seen that the mechanics of collapse are different for small and large size beams. When the beam is large enough, the structure fails as soon as the damage criterion is reached at the bottom midpoint of the beam and a vertical crack suddenly appears. When the size is small enough, damage develops over an extensive area before a collapse mechanism is formed and failure is due to the development in the center of the beam of a perfect hinge. As size increases, the observed mechanism tends from one limit case to the other. This is the source for structural size effect.

As it was observed in previous sections, in unnotched beams of medium sizes an area of low value damage develops at the bottom midsection of the beam prior to the strain localization. Note that this area is nonexistent in the larger beams and becomes bigger as size decreases. Note also that even though the damaged area can become large when size decreases, strain localization in a narrow band is properly taking place in the computed strain field for all the sizes. As the energy dissipated in the plastic limit is proportional to the inelastic strain developed, the correct strain localization pattern shows that energy is correctly dissipated even if the damaged zone is more extensive.

The peak load of both the small and large limit cases can be readily computed. Statics show that the maximum bending moment under three-point bending occurs at the midsection of the beam

$$M_{max} = \frac{1}{4} P_u \, 2.5D = \frac{5}{8} P_u D \tag{27}$$

In the small size limit, the peak load can be derived from the limit analysis of the beam. The structure fails when a hinge develops at the midsection of the beam. As only tensile damage is considered, the maximum bending moment that the cross section can sustain is attained when the entire section of the beam carries the tensile maximum stress f_t. With this stress distribution, the neutral axis is located at the top of the mid cross section and the bending moment of the beam at the midsection is

$$M_u = \frac{1}{2} D^2 b f_t \tag{28}$$

Therefore, equating (32)and (33), the peak load P_u of the beam for the small limit case is

$$P_u = \frac{4}{5} D b f_t \tag{29}$$

And the corresponding nominal strength σ_{N_u} is

$$\sigma_{N_u} = \frac{P_u}{Db} = \frac{4}{5} f_t \tag{30}$$

Notice that in the small limit case the peak load P_u is linear with respect the size D and the nominal strength σ_{N_u} is constant.

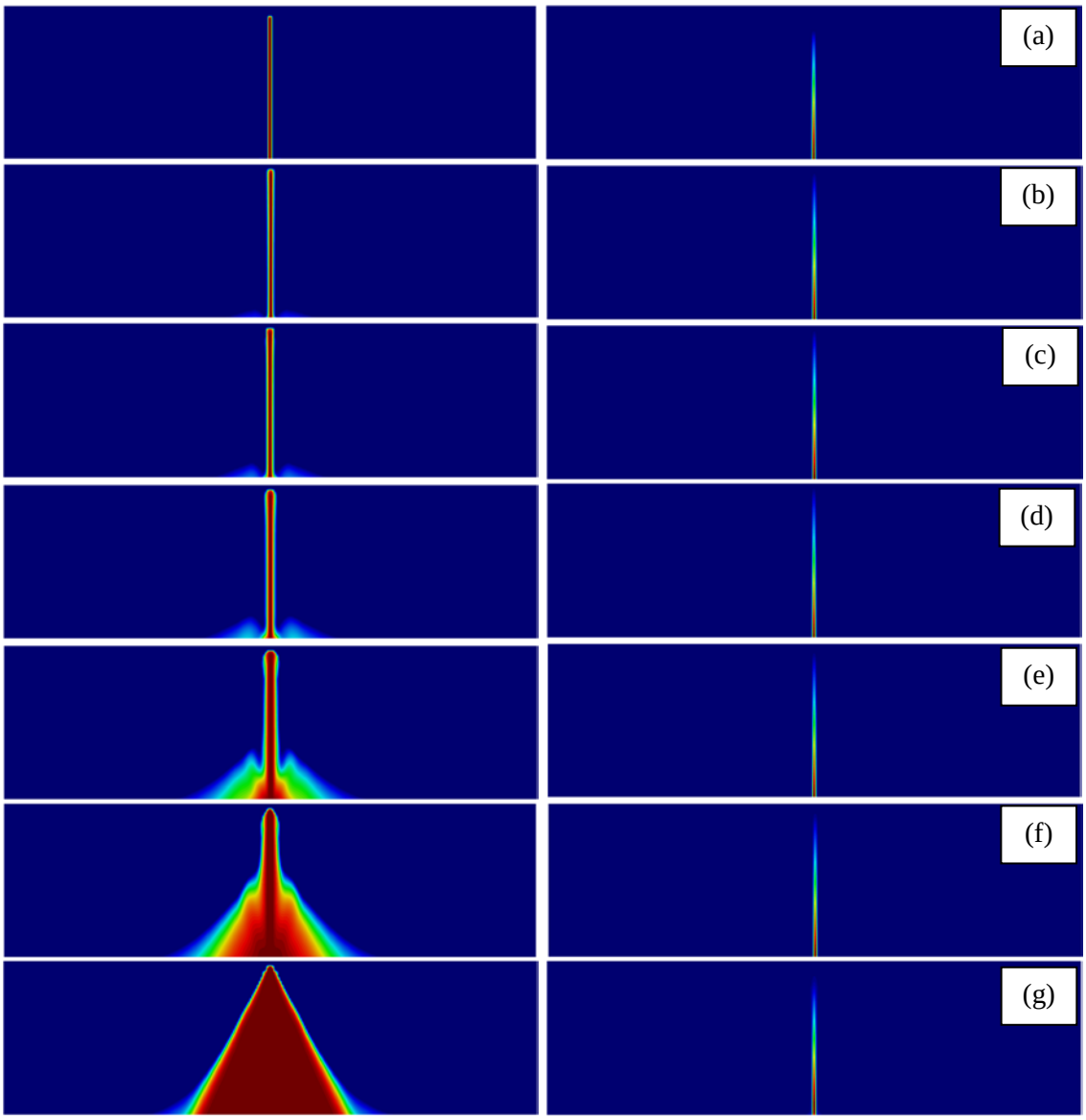

Figure 30. Variation of the (left) damage and (right) maximum principal strain contours of the unnotched beam for scales (a) 10, (b) 1, (c) 0,5, (d) 0.25, (e) 0.05, (f) 0.01 and (g) 10^{-4}

In the large size limit a perfectly brittle failure occurs and a linear elastic analysis of the beam can be considered. Considering the Euler-Bernoulli beam theory, a bending moment M acting on a D x b rectangular section produces a maximum tensile stress located at the bottom equal to

$$\sigma_{max} = 6 \frac{M}{D^2 b} \tag{31}$$

Therefore, for $M = M_{max}$ in Eq. (32)

$$\sigma_{max} = 3.75 \frac{P}{Db} \tag{32}$$

As structural failure occurs when $\sigma_{max} = f_t$, the peak load P_u of the beam in the large limit case is

$$P_u = \frac{4}{15} D b f_t \tag{33}$$

And the corresponding nominal strength σ_{N_u} is

$$\sigma_{N_u} = \frac{P_u}{Db} = \frac{4}{15} f_t \tag{34}$$

Notice that in the large limit case the peak load P_u is also linear with respect the size D and the nominal strength σ_{N_u} is constant.

Figure 31 shows the predictions of the nominal strength with respect the beam size that are obtained with the computational FE model. On the one hand, it can be seen that for small sizes the nominal strength tends towards the limit set by limit analysis. On the other hand, for big sizes the nominal strength reaches the value corresponding to perfectly brittle failure. Note that the large scale limit is not tending exactly to the limit predicted by the linear elastic analysis. This is because the beam has a span-to-depth ratio of 2.5, which is too small for the Euler-Bernoulli theory to be fully valid. Nonetheless, the large scale limit predicted with the Euler-Bernoulli assumptions is a good approximation (7% off).

In Figure 32 the computed ultimate load vs beam depth results are shown. As noted in the introduction, the nominal strength σ_{N_u} is in fact an indirect way of describing the peak load P_u reached by the structure. The phenomenon is described in a much clearer way using the nominal strength.

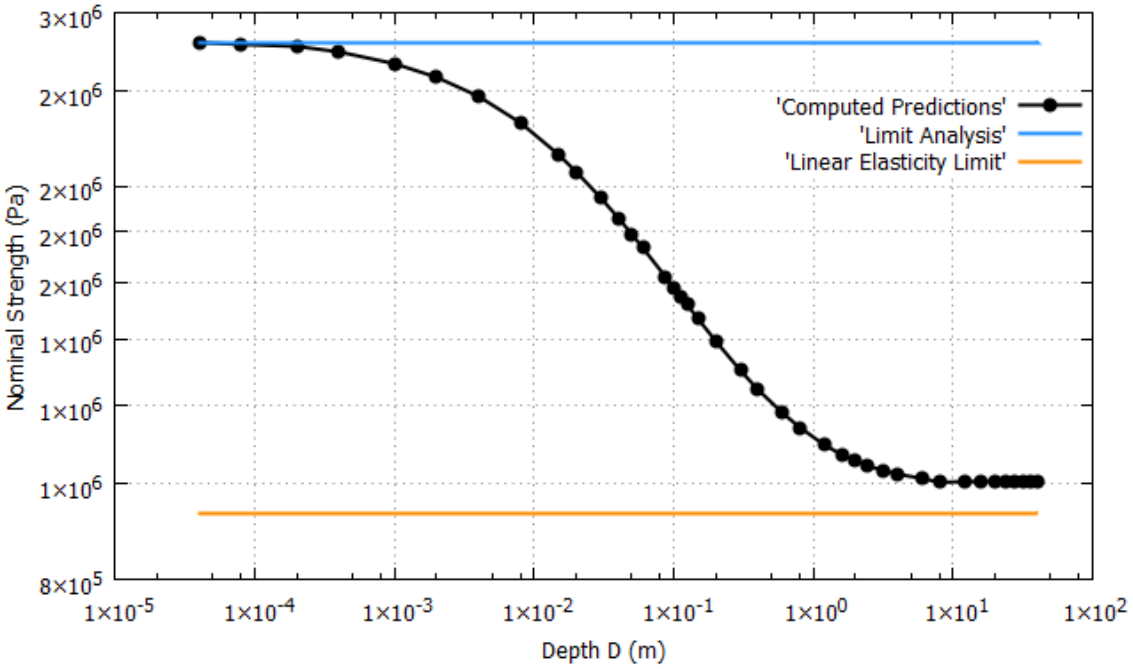

Figure 31. Computed predictions of the nominal strength vs beam depth for the unnotched beam

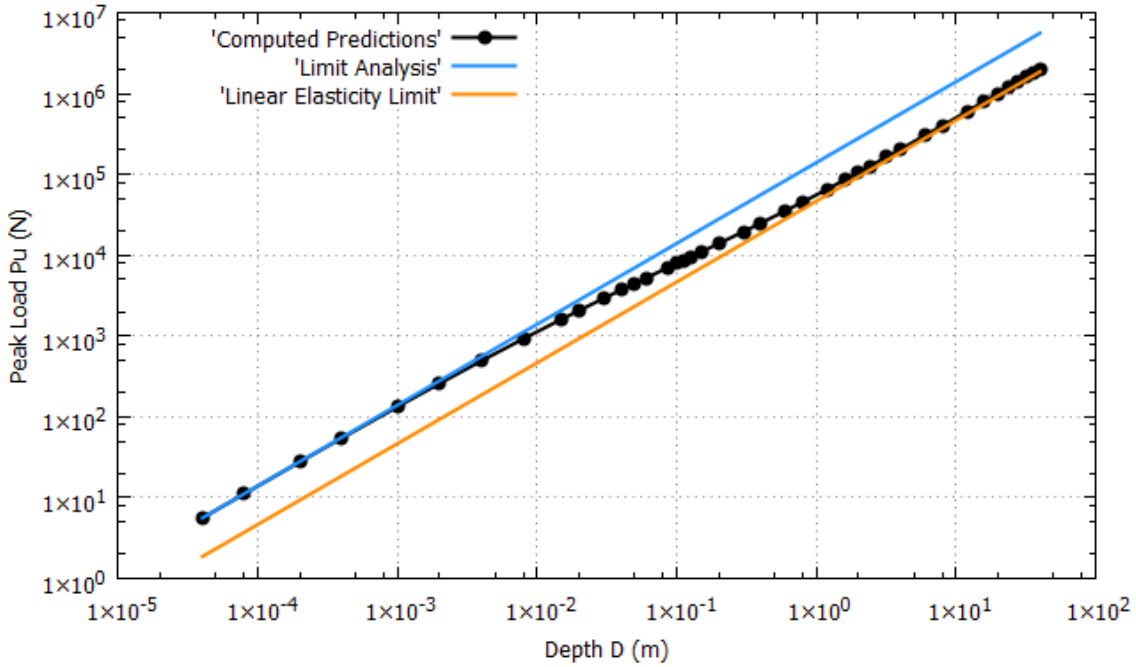

Figure 32. Computed predictions of the peak load vs beam depth for the unnotched beam

Notched beam size effect predictions

Figure 33 depicts damage and maximum principal strain contour fills obtained for several sizes of the notched beam. The same mesh as the one used in the simulations of Section 5.1, shown in Figure 34a, is employed for scales lower or equal than 20. For larger cases a finer mesh, detailed in Figure 34b, is used, where the FE size is $1.25 \cdot 10^{-4} D$ near the crack tip, resulting in a 121026 element mesh.

It can be seen that the extension of the area affected by damage grows as the size diminishes. It can be noticed once more that even though the damaged area becomes large for smaller sizes, strain localization in a narrow band is properly taking place in the computed strain field. For large beams a very brittle failure occurs, caused by a vertical crack starting at the tip of the notch. In that situation the structural failure is influenced in a determining way by the stresses concentrating around the notch, which need to be computed accurately. For this reason, a mesh refinement of the area near the tip of the notch is necessary for the larger cases. For small enough scales a perfect hinge is developed in the midsection of the beam, analogously to the unnotched case.

The peak load of the small limit case can be calculated from limit analysis using the same method as for the unnotched beam. The structure fails when a hinge develops at the midsection of the beam. Considering that the notch has a length of λD, the maximum bending moment at the midsection is

$$M_u = \frac{1}{2}(1-\lambda)^2 D^2 b f_t \tag{35}$$

Therefore, the peak load P_u of the beam for the small limit case is

$$P_u = \frac{4}{5}(1-\lambda)^2 D b f_t \tag{36}$$

And the corresponding nominal strength σ_{N_u} is

$$\sigma_{N_u} = \frac{P_u}{Db} = \frac{4}{5}(1-\lambda)^2 f_t \tag{37}$$

Notice that again the peak load P_u is linear with respect the size D and the nominal strength σ_{N_u} is constant.

The peak load of the large limit case cannot be correctly computed considering the Euler-Bernoulli beam theory as in the unnotched case because the effect of the stress concentration around the notch tip is not taken into account. In situations where stress singularities exist, a failure criterion expressed in terms of stress is not adequate. In such cases, an energy failure criterion such as the one introduced in LEFM becomes relevant.

In the LEFM approach the expected relation of the nominal strength for two sizes A and B is

$$\frac{\left(\sigma_{N_u}\right)_A}{\left(\sigma_{N_u}\right)_B} = \left(\frac{D_A}{D_B}\right)^{-\frac{1}{2}} \tag{38}$$

And the predicted relation of the corresponding peak loads is

$$\frac{(P_u)_A}{(P_u)_B} = \left(\frac{D_A}{D_B}\right)^{\frac{1}{2}} \tag{39}$$

In Figure 35 the computed predictions of the nominal strength with respect the beam size for the notched case are depicted. For small sizes the nominal strength reaches the limit set by limit analysis. It can be seen that for large sizes the nominal strength follows the behavior specified by LEFM theory.

In Figure 36 the computed predictions are shown in terms of peak load vs structural size. Once more the size effect phenomenon is revealed in a clearer way with the use of the nominal strength.

The aptness of the predictions computed with the model can be assessed by examining their fitting with respect Bazant's size effect law. To adjust the parameters of Bazant's law with the produced numerical data, a nonlinear least squares fitting procedure is performed. The result is shown in Figure 37.

Three different functions are considered for adjusting the data. First, Bazant's original law is considered

$$\sigma_{N_u} = B f_t \left[1 + \left(\frac{D}{D_0}\right)\right]^{-\frac{1}{2}} \tag{40}$$

The fitted parameters obtained are $B = 0.43987$ and $D_0 = 0.14895\, m$. It can be seen that Bazant's original law does not fit correctly the data for the whole range of depths; in particular, it does not fit well the regions corresponding to small and intermediate specimen sizes. This issue has already been discussed in reference [1] when considering a large range of sizes. As a remedy, Bazant's general law has been proposed

$$\sigma_{N_u} = B f_t \left[1 + \left(\frac{D}{D_0}\right)^r\right]^{-\frac{1}{2r}} \tag{41}$$

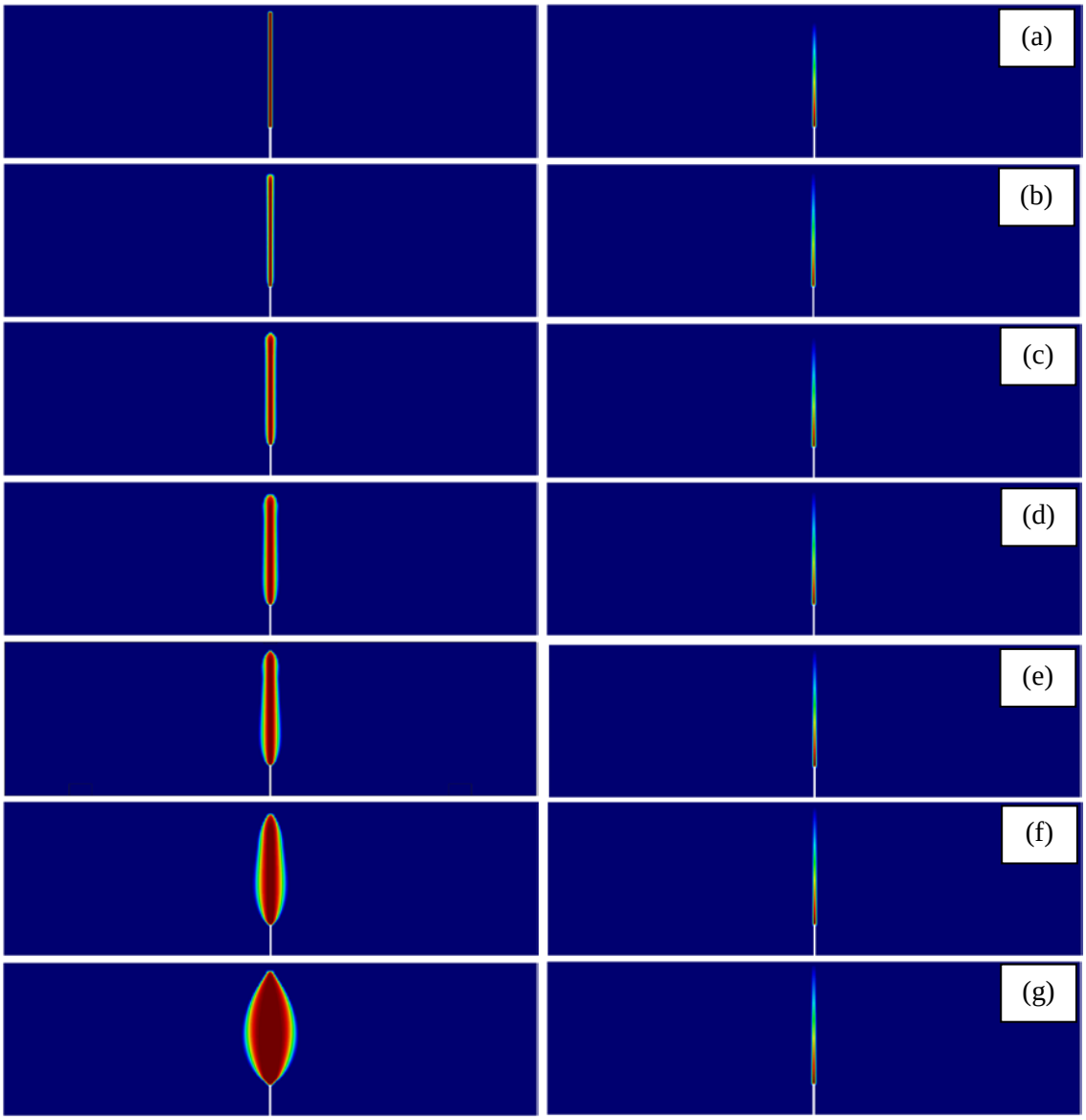

Figure 33. Variation of the (left) damage and (right) maximum principal strain contours of the notched beam for scales (a) 20, (b) 1, (c) 0,25, (d) 0.125, (e) 0.05, (f) 0.01 and (g) 10^{-4}

The fitted parameters obtained are $B = 0.51165$, $D_0 = 0.13819\, m$ and $r = 0.51318$. Note that $D_0 = 0.5084L$. It can be observed that Bazant's general law fits much better the computed predictions over the whole domain than the original law. The level of adjustment with the numerical predictions is notable as the size range considered here is very extensive, spreading over more than 6 orders of magnitude. In reference [1] it is already pointed out that parameters r close to 0.5 fit better data which is extended over a wide range of sizes.

Finally, let us consider the fitting of the computed predictions with the power law

$$\sigma_{N_u} = AD^m \tag{42}$$

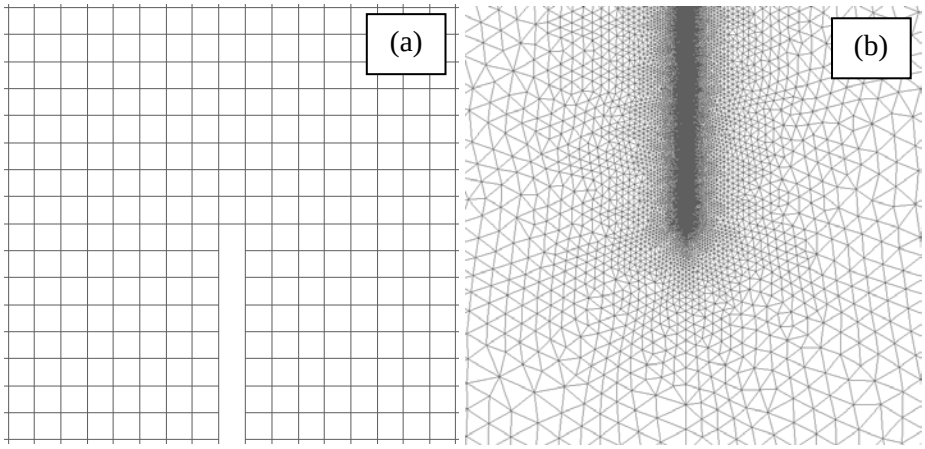

Figure 34. Detail of the mesh used for the notched beam size effect predictions around the tip of the notch with (a) 22464 quadrilateral elements and (b) 121026 triangular elements

The fitted parameters are $A = 322760.818$ and $m = -0.25189$ and the corresponding curve is also shown in Figure 37. It can be clearly seen that the power law fits very poorly the results. This clearly shows that, as it is stressed out in references [3, 4, 10], size effect cannot be modelled with the power law and that the phenomenon in fact involves a characteristic size D_0, related to the material characteristic length L.

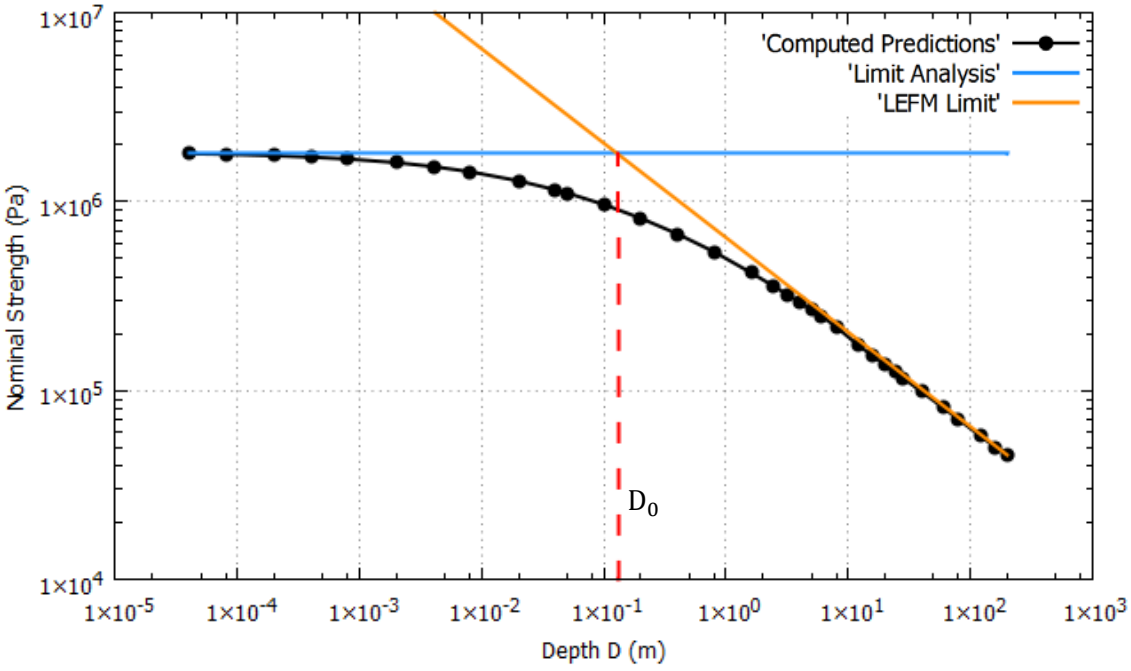

Figure 35. Computed predictions of the nominal strength vs beam depth for the notched beam

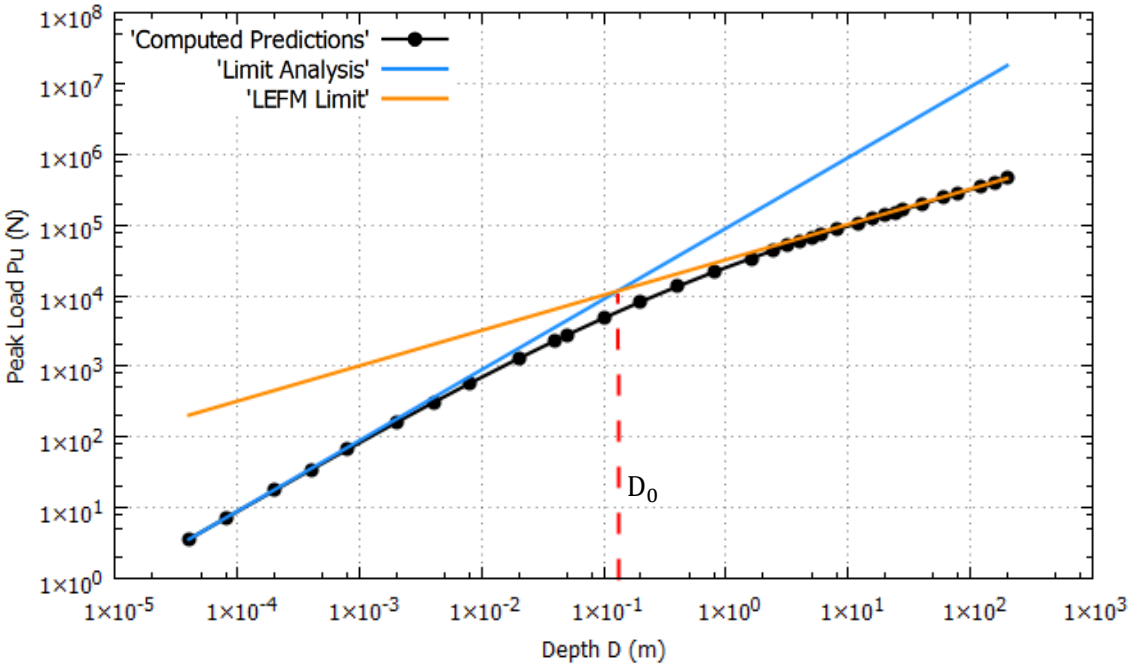

Figure 36. Computed predictions of the peak load vs beam depth for the notched beam

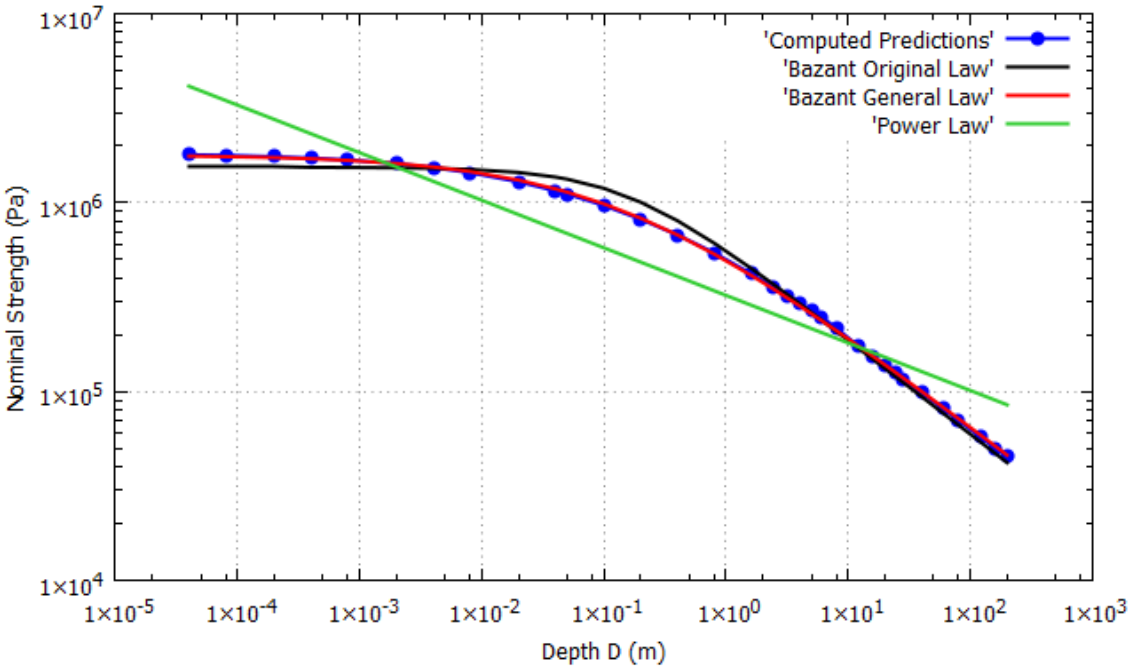

Figure 37. Fitting of the numerical predictions with respect Bazant's size effect law

The size effect phenomenon also involves a change in the ductility and the post-peak behavior of the specimens. Figure 38 shows the nominal stress vs normalized CMOD curve (nominal stress being also a measure of force normalized with respect structural size) of the simulations performed for the notched beams. It can be seen how the behavior of the beams changes from ductile to brittle when size increases. Once properly normalized, the peak load and the energy dissipated in the failure process is comparatively smaller in larger structures. The collapse in larger specimens happens closer to the peak load while in smaller ones the post-peak curve descends much more slowly. It is observed that the nonlinear regime starts before the peak load

is attained, particularly for more ductile behavior. Therefore, it is shown that, besides considering with accuracy the effect that the phenomenon has on load capacity, the computational model is also able of reproducing the ductility changes originated by variations in structural size.

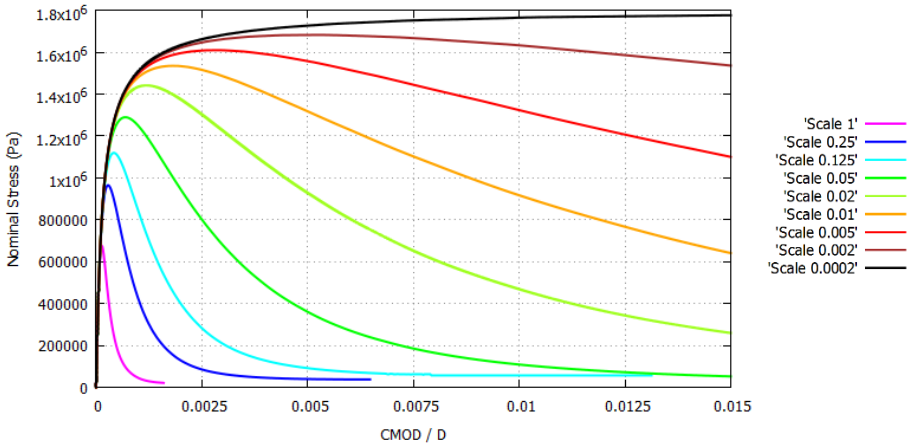

Figure 38. Normalized force-CMOD curves for various scales of the notched beam

9. Conclusions

In this work, the phenomenon of structural size effect is addressed, and experimental evidence, theoretical predictions and computational modelling using FEs are assessed against each other. Quasi-brittle failure is accurately modelled with a classical local isotropic Rankine damage constitutive law. The correct dissipation of fracture energy in the crack, fundamental to appropriately consider size effect, is enforced in conjunction with the crack band approach. The model is used together with an enhanced accuracy mixed **ε/u** finite element formulation to provide results without spurious mesh bias.

The simulation of several experimental campaigns, where the phenomenon is investigated in mode I and mixed mode I and II, is carried out. The performance of the model in modelling size effect is shown in notched and unnotched beams.

It is observed that:

- The proposed local isotropic damage constitutive model is fit for the numerical simulation of structural size effect.
- Results documented in several experimental campaigns where the phenomenon is carefully studied are accurately reproduced in 2D and 3D.
- The results obtained with the mixed FE formulation are free from the spurious mesh dependency in terms of computed crack trajectory which is typical of standard FEs.
- The dominant influence of size effect in quasi-brittle materials is the release of stored energy as the crack progresses in the structure
- Bazant's size effect law is followed with exactitude over a wide range using the proposed model.

From these, it is concluded that the proposed isotropic damage model, used together with the mixed finite element formulation, is suitable for reproducing size effect in quasi-brittle materials in mode I and mixed mode I and II loading with mesh objectivity and without the need of using auxiliary crack tracking techniques.

10. **Acknowledgements**

Financial support from the Spanish Ministry of Economy and Business via the ADaMANT (Computational Framework for Additive Manufacturing of Titanium Alloy) project (Proyectos de I + D (Excelencia) DPI2017-85998-P) is gratefully acknowledged. The support provided by the Spanish Ministry of Education to Mr. Gabriel Barbat via the FPU program is also acknowledged.

11. **References**

[1] Z. Bazant and J. Planas, Fracture and Size Effect in Concrete and Other Quasibrittle Materials, Boca Raton: CRC Press, 1998.

[2] ACI, Building Code Requirements for Structural Concrete (ACI 318-19), 2019.

[3] Z. Bazant, "Size effect," *International Journal of Solids and Structures,* vol. 37, pp. 69-80, 2000.

[4] Z. Bazant, "Size effect on structural strength: a review," *Archive of Applied Mechanics,* vol. 69, pp. 703-725, 1999.

[5] Y. Rashid, "Ultimate strength analysis of prestressed concrete pressure vessels," *Nuclear Engineering and Design,* vol. 7, no. 4, pp. 334-344, 1968.

[6] Z. Bazant and B. Oh, "Crack band theory for fracture of concrete," *Matériaux et Constructions,* vol. 16, no. 3, pp. 155-177, 1983.

[7] M. Cervera and J.-Y. Wu, "On the conformity of strong, regularized, embedded and smeared discontinuity approaches for the modelling of localized faillure in solids," *International Journal of Solids and Structures,* vol. 71, pp. 19-38, 2015.

[8] J. Wu and M. Cervera, "On the equivalence between traction- and stress-based approaches for the modeling of localized failure in solids," *Journal of the Mechanics and Physics of Solids,* vol. 82, pp. 137-163, 2015.

[9] Z. Bazant, "Fracture in Concrete and Reinforced Concrete," in *Mechanics of Geomaterials,* 1985, pp. 259-303.

[10] Z. Bazant and E.-P. Chen, "Scaling of Structural Failure," Sandia Report SAND96-2948, Albuquerque, New Mexico, 1997.

[11] M. Cervera and M. Chiumenti, "Size effect and localization in J2 plasticity," *International Journal of Solinds and Structures,* vol. 46, pp. 3301-3312, 2009.

[12] M. Cervera and M. Chiumenti, "Smeared crack approach: back to the original track," *Int. J. Numer. Anal. Meth. Geomech.,* vol. 30, pp. 1173-1199, 2006.

[13] M. Cervera and M. Chiumenti, "Mesh objective tensile cracking via a local continuum damage model and a crack tracking technique," *Computer Methods and Applied Mechanics in Engineering,* vol. 196, no. 1-3, pp. 304-320, 2006.

[14] R. Peerlings, R. de Borst, W. Brekelmans and J. de Wree, "Gradient enhanced damage for quasi brittle materials," *International Journal for Numerical Methods in Engineering,* vol.

39, pp. 3391-3403, 1996.

[15] R. de Borst and C. Verhoosel, "Gradient damage vs phase-field approaches for fracture: Similarities and differences.," *Comput. Methods Appl. Mech. Engrg.,* vol. 312, pp. 78-94, 2016.

[16] R. Peerlings, M. Geers, R. de Borst and W. Brekelmans, "A critical comparison of nonlocal and gradient-enhanced softening continua," *International Journal of Solids and Structures,* vol. 38, pp. 7723-7746, 2001.

[17] Z. Bazant and G. Pijaudier-Cabot, "Nonlocal continum damage, localization instabilities and convergence," *Journal of Engineering Mechanics* , no. 55, pp. 287-293, 1988.

[18] C. Miehe, F. Welschinger and M. Hofacker, "Thermodynamically consistent phase-field models of fracture: Variational principles and multi-field FE implementations," *International Journal for Numerical Methods in Engineering,* vol. 83, pp. 1273-1311, 2010.

[19] C. Miehe, L.-M. Schänzel and H. Ulmer, "Phase field modeling of fracture in multi-physics problems. Part I. Balance of cracks surface and failure criteria for brittle crack propagation in thermo-elastic solids," *Computer Methods in Applied Mechanics and Engineering,* vol. 294, pp. 449-485, 2015.

[20] J. Vignollet, S. May, R. de Borst and C. Verhoosel, "Phase-field model for brittle and cohesive fracture," *Meccanica,* vol. 49, pp. 2587-2601, 2014.

[21] G. Nguyen, C. Nguyen, P. Nguyen, H. Bui and L. Shen, "A size-dependent constitutive modelling framework for localized faillure analysis," *Comput. Mech.,* vol. 58, pp. 257-280, DOI 10.1007/s00466-016-1293-z, 2016.

[22] J. Wu, "A geometrically regularized gradient-damage model with energetic equivalence," *Computer Methods in Applied Mechanics and Engineering,* vol. 328, pp. 612-637, 2018.

[23] J.-Y. Wu, "A unified phase-field theory for the mechanics of damage and quasi-brittle failure," *Journal of the Mechanics and Physics of Solids,* vol. 103, pp. 72-99, 2017.

[24] J.-Y. Wu and V. Nguyen, "A length scale insensitive phase-field damage model for brittle fracture," *Journal of the Mechanics and Physics of Solids,* vol. 119, pp. 20-42, 2018.

[25] D.-C. Feng and J.-Y. Wu, "Phase-field regularized cohesive zone model (CZM) and size effect of concrete," *Engineering Fracture Mechanics,* vol. 197, pp. 66-79, 2018.

[26] M. Cervera, M. Chiumenti and R. Codina, "Mixed stabilized finite element methods in nonlinear solid mechanics. Part I: Formulation," *Computer Methods in Applied Mechanics and Engineering,* vol. 199, no. 37-40, pp. 2559-2570, 2010.

[27] M. Cervera, M. Chiumenti and R. Codina, "Mixed stabilized finite element methods in nonlinear solid mechanics. Part II: Strain localization," *Computer Methods in Applied Mechanics and Engineering,* vol. 199, no. 37-40, pp. 2571-2589, 2010.

[28] M. Cervera, M. Chiumenti, L. Benedetti and R. Codina, "Mixed stabilized finite element methods in nonlinear solid mechanics. Part III: Compressible and incompressible plasticity," *Computer Methods in Applied Mechanics and Engineering,* vol. 285, no. 0, pp.

752-775, 2015.

[29] M. Cervera, G. Barbat and M. Chiumenti, "Finite element modelling of quasi-brittle cracks in 2D and 3D with enhanced strain accuracy," *Computational Mechanics,* vol. 60, no. 5, pp. 767-796, 2017.

[30] G. Barbat, M. Cervera and M. Chiumenti, "Appraisement of planar, bending and twisting cracks in 3D with isotropic and orthotropic damage models," *International Journal of Fracture,* vol. 210, no. 1-2, pp. 45-79, 2018.

[31] G. Vlachakis, M. Cervera, G. Barbat and S. Saloustros, "Out-of-plane seismic response and faillure mechanism of masonry structures using finite elements with enhanced strain accuracy," *Engineering Faillure Analysis,* vol. 97, pp. 534-555, 2019.

[32] M. Cervera, G. Barbat and M. Chiumenti, "Architecture of a multi-crack model with full closing, reopening and sliding capabilities," *Computational Mechanics,* DOI:10.1007/s00466-020-01836-y , 2020.

[33] Z. Bazant and Q. Yu, "Universal Size Effect Law and Effect of Crack Depth on Quasi-Brittle Structure Strength," *Journal of Engineering Mechanics,* vol. 135, no. 2, pp. 78-84, 2009.

[34] N. Jones, Structural impact, Cambridge: Cambridge University Press, 1989.

[35] R. Oshiro and M. Alves, "Scaling impacted structures," *Archive of Applied Mechanics,* vol. 74, pp. 130-145, 2004.

[36] M. Alves, R. Oshiro, M. Calle and L. Mazzariol, "Scaling and structural impact," *Procedia Engineering,* vol. 173, pp. 391-396, 2017.

[37] J. Oliver, M. Cervera, S. Oller and J. Lubliner, "Isotropic damage models and smeared crack analysis of concrete," *II int. conference on computer aided analysis and design of concrete,* 1990.

[38] L. Benedetti, M. Cervera and M. Chiumenti, "3D modelling of twisting cracks under bending and torsion skew notched beams," *Engineering Fracture Mechanics,* vol. 176, pp. 235-256, 2017.

[39] I. Babuska, "Error-bounds for finite element method," *Numerisch Mathematik,* vol. 16, pp. 322-333, 1971.

[40] D. Boffi, F. Brezzi and M. Fortin, "Mixed Finite Element Methods and Applications," *Springer,* 2013.

[41] F. Brezzi, "On the existence, uniqueness and approximation of saddle-point problems arising from lagrangian multipliers," *ESAIM: Mathematical Modelling and Numerical Analysis - Modélisation Mathématique et Analyse Numérique,* vol. 8, no. R2, pp. 129-151, 1974.

[42] R. Codina, "Stabilization of incompressibility and convection through orthogonal sub-scales in finite element methods," *Computer Methods in Applied Mechanics and Engineering ,* vol. 190, pp. 1579-1599, 2000.

[43] D. Grégoire, L. Rojas-Solano and G. Pijaudier-Cabot, "Faillure and size effect for notched and unnotched concrete beams," *International Journal for Numerical and Analytical Methods in Geomechanics,* vol. 37, pp. 1434-1452, 2013.

[44] C. Hoover, Z. Bazant, J. Vorel, R. Wendner and M. Hubler, "Comprehensive concrete fracture tests: Description and results," *Engineering Fracture Mechanics,* vol. 114, pp. 92-103, 2013.

[45] V. Garcia-Alvarez, R. Gettu and I. Carol, "Analysis of mixed-mode fracture in concrete using interface elements and a cohesive crack model," *Sadhana,* vol. 37, no. 1, pp. 187-205, 2012.

[46] M. Cervera, C. Agelet de Saracibar and M. Chiumenti, "COMET: Coupled Mechanical and Thermal Analysis. Data Input Manuel, Version 5.0, Technical report IT-308. Available from http://www.cimne.upc.edu," 2002.

[47] A. Coll, R. Ribo, M. Pasenau, E. Escolano, J. S. Perez, A. Melendo, A. Monros and J. Garate, "GiD: the personal pre and post-processor User Manual," *CIMNE, Technical University of Catalonia,* p. <http://gid.cimne.upc.ed>, 2002.

[48] E. Rodrigues, O. Manzoli, L. Bitencourt and T. Bittencourt, "2D mesoscale model for concrete based on the use of interface element with a high aspect ratio," *International Journal of Solids and Structures,* Vols. 94-95, pp. 112-124, 2016.

[49] M. Vassaux, C. Oliver-Leblond, B. Richard and F. Ragueneau, "Beam-particle approach to model cracking and energy dissipation in concrete: Identification strategy and validation," *Cement and Concrete Composites,* vol. 70, pp. 1-14, 2016.

[50] J. Elias, "Boundary Layer Effect on Behavior of Discrete Models," *Materials,* vol. 10, no. 2, p. 157, 2017.

[51] S. Seetharam, E. Laloy, A. Jivkov, L. Yu, Q. Phung, N. Pham, B. Kursten and F. Druyts, "A mesoscale framework for analysis of corrosion induced damage of concrete," *Construction and Building Materials,* vol. 216, pp. 347-361, 2019.

[52] R. Wendner, J. Vorel, J. Smith, C. Hoover, Z. Bazant and G. Cusatis, "Characterization of concrete failure behavior: a comprehensive experimental database for the calibration and validation of concrete models," *Materials and Structures,* vol. 48, pp. 3603-3626, 2015.

[53] P. Havlasek, P. Grassl and M. Jirasek, "Analysis of size effect on strength of quasi-brittle materials using integral-type nonlocal models," *Engineering Fracture Mechanics,* vol. 157, pp. 72-85, 2016.

[54] E. Lorentz, "A nonlocal damage model for plain concrete consistent with cohesive fracture," *International Journal of Fracture,* vol. 207, no. 2, pp. 123-159, 2017.

[55] J. Klon and V. Vesely, "Modelling of size and shape of damage zone in quasi-brittle notched specimens – analytical approach based on fracture-mechanical evaluation of loading curves," *Frattura ed Integrità Strutturale,* vol. 39, pp. 17-28, 2017.

[56] I. Marzec and J. Bobinski, "On Some Problems in Determining Tensile Parameters of Concrete Model from Size Effect Tests," *Polish Maritime Research,* vol. 102, no. 2, pp. 115-125, 2019.

[57] M. Gutierrez and R. De Borst, "Deterministic and stochastic analysis of size effects and damage evolution in quasi-brittle materials," *Archive of Applied Mechanics*, vol. 69, pp. 655-676, 1999.